Paul Zorn, Bsc.

Characterization and stability investigation of Platinum and Palladium free cathode catalysts for a direct ethanol fuel cell

MASTERARBEIT

zur Erlangung des akademischen Grades

Diplom-Ingenieur

Masterstudium Technische Chemie

eingereicht an der

Technischen Universität Graz

Betreuer

Assoc.Prof. Dipl.-Ing. Dr.techn., Viktor Hacker
Dipl.-Ing. Grimmer Ilena, BSc

Institut für Chemische Verfahrenstechnik und Umwelttechnik

Graz, Monat und Jahr

Characterization and stability investigation of Platinum and Palladium free catalysts for a direct ethanol fuel cell

für
Herrn Paul Zorn

Aufgabenstellung

Direkt Ethanol Brennstoffzellen (engl.: direct ethanol fuel cells, DEFC) erlauben den Einsatz des großtechnisch verfügbaren und gering giftigen Ethanols zur Strom- und Wärme-Bereitstellung. Eine Ethanol Produktion aus erneuerbaren Ressourcen erlaubt es den Kohlenstoffkreislauf zu schließen, wodurch sich die Möglichkeit einer klimaneutralen Energieumwandlung bietet.

Ziel dieser Arbeit ist es platinfreie Kathodenkatalysatoren zu charakterisieren und ihre Eignung für die Katalyse der Sauerstoffreduktion einer DEFC zu untersuchen. Dafür werden drei verschiedene Katalysatoren hergestellt und ex-situ also auch in-situ verglichen. Die Ergebnisse liefern die Grundlage für die nachfolgende Leistungs- und Stabilitätsverbesserung, sowie Erkenntnisse über vorteilhafte Parameter zum Betrieb der Einzel- und Vollzelle.

EIDESSTATTLICHE ERKLÄRUNG

Ich erkläre an Eides statt, dass ich die vorliegende Arbeit selbstständig verfasst, andere als die angegebenen Quellen/Hilfsmittel nicht benutzt, und die den benutzten Quellen wörtlich und inhaltlich entnommenen Stellen als solche kenntlich gemacht habe.

Graz, am …… ……

(Unterschrift)

Englische Fassung:

STATUTORY DECLARATION

I declare that I have authored this thesis independently, that I have not used other than the declared sources / resources, and that I have explicitly marked all material which has been quoted either literally or by content from the used sources.

Graz, …… ……

date (signature)

Kurzfassung

Biotreibstoffe werden einen wirksamen Beitrag zur Erreichung der Klimaziele leisten, wenn sie in angemessenen Umfang und reglementiert produziert werden. Bioethanol wird bereits großtechnisch hergestellt und derzeit als Primärtreibstoff oder Treibstoffzusatz für den Verbrennungsmotor eingesetzt. Die Verwendung in Direkt-Ethanol-Brennstoffzellen könnte zukünftig eine effizientere Alternative der Energieumwandlung darstellen und den Anwendungsbereich von Bioethanol erweitern. Die hohe Energiedichte und niedrige Toxizität machen Ethanol, in Kombination mit der guten Skalierbarkeit von Brennstoffzellsystemen, zu einem vielversprechenden Energieträger und Energiespeicher für mobile und portable Anwendungen.

Derzeitige Direkt-Ethanol-Brennstoffzellen verwenden Katalysatoren aus seltenen Metallen wie Platin und Palladium. Ziel dieser Arbeit war es daher, drei alternative Kathodenkatalysatoren hinsichtlich ihrer Eignung für den Einsatz in einer Direkt-Ethanol-Brennstoffzelle zu untersuchen. Dafür wurden zwei Perowskite und ein Silber-basierender Katalysator aus den entsprechenden Nitrat-Salzen hergestellt. Die physikalischen Katalysatoreigenschaften wurden mittels SEM und XRD untersucht. Dadurch konnten Morphologieunterschiede und die Phasenreinheit der hergestellten Katalysatoren nachgewiesen werden. Zum Literaturvergleich der katalytischen Aktivität wurden ex-situ Messungen mithilfe einer RDE-Analyse (engl. rotating-disc electrode, RDE) durchgeführt. Bei der in-situ Analyse wurden Polarisationskurven der Kathoden unter unterschiedlichen Operationsbedingungen aufgenommen. Dementsprechend wurden in Halbzellen Untersuchungen die Elektrolytkonzentration, die Binderkonzentration, die Betriebstemperatur und der Sauerstoffpartialdruck verändert. Zudem wurde die Stabilität der Kathoden mit und ohne Ethanolzusatz in Langzeitmessungen untersucht. Im alkalischen Medium zeigten alle hergestellten Elektroden eine sehr gute Langzeitstabilität über mehreren hundert Stunden. Nach der Zugabe von Ethanol, konnten nur die Perowskit-basierenden Elektroden vergleichbar stabile Funktion beibehalten. Vollzellenmessungen bestätigten die prinzipielle Eignung der Perowskit-basierenden Kathoden unter realen Betriebsbedingungen.

Abstract

Biofuels, like ethanol, contribute its part to achieve climate goals in a sustainable way, if they are produced and used in a proper and regulated way. Nowadays, ethanol-biofuels are already produced in large-scale and used in combustion engines for mobility. The usage of ethanol as alternative fuel to H_2 in a fuel cell, a so-called Direct Ethanol Fuel Cell (DEFC), has the future potential to reach a more efficient energy conversion and to enhance the field of ethanol application. Due to the high energy density and low toxicity of the fuel, as well as the good scalability of fuel cells, an implementation as power supply for portable and mobile applications seems beneficial.

State-of-the-art DEFC anode and cathode electrodes use precious metals like platinum and palladium as catalysts. The aim of this work was to characterize and analyze alternative cathode catalysts regarding their suitability for application in a DEFC. Therefore, two perovskites and one silver-based catalyst were manufactured from nitrate precursors. To analyze the physical properties of the prepared catalysts, scanning electron microscopy (SEM) and X-ray diffraction investigations were performed. It revealed morphology differences between the catalyst and the phase purity. Rotating disk electrode measurements were executed (RDE) to investigate the cathodes performance ex-situ and to compare it with literature data. The electrodes, which were produced from these catalysts, were used for in-situ investigations. During that, a series of half-cell experiments was performed, aiming to investigate the influence of the electrolyte concentration, the operation temperature, the binder concentration and the partial pressure of oxygen on the cathode´s performance. In addition long-term measurements should reveal the stability of the cathodes with and without ethanol. In alkaline media, all electrodes showed a remarkable stability over a couple hundreds of hours. The perovskite-based electrodes were able to maintain a similar stability after the addition of ethanol. The full-cell experiment conformed the principle suitability of the prepared cathodes to operate under real working conditions.

Content

1 Introduction

1.1 Environmental aspects of alcohol fuel cell technology

Fuel cells are efficient energy converters with low emissions. They are used to produce electricity and heat for households, in the transport sector, for portable applications and backup power devices. A main driving force for implementation of fuel cells is the targeted change to sustainable and high efficient technologies to handle global warming issues. 2016 has been the hottest year in 137 years of modern recordkeeping, which began in the 19th century with the implementation of improved standardized instrumentation. Even though this record is also caused by strong 2015-2016 El Niño (a weather phenomenon in the Equatorial Pacific), the contribution of a strong global warming trend cannot be neglected. 16 of the 17 hottest years in between 1880 to 2017 have occurred since 2000 [1]. Global warming is in general strongly related to the growth of human population as well as industry and its associated CO_2 release. Svante Arrhenius was one of the first who quantified the carbon dioxide contribution to the greenhouse effect. He published his conclusions in the year 1896 [2]. In later works he suggested that the anthropogenic burning of fossil fuels can be a potentially source of carbon dioxide in the atmosphere. Since the industrial revolution, fossil fuels have been used to handle increasing energy demands what results in a significant release of the greenhouse active CO_2. Hereupon, carbon dioxide emissions had been continuously risen what leads to an increasing temperature (seen in the diagram below), as expected already by Arrhenius.

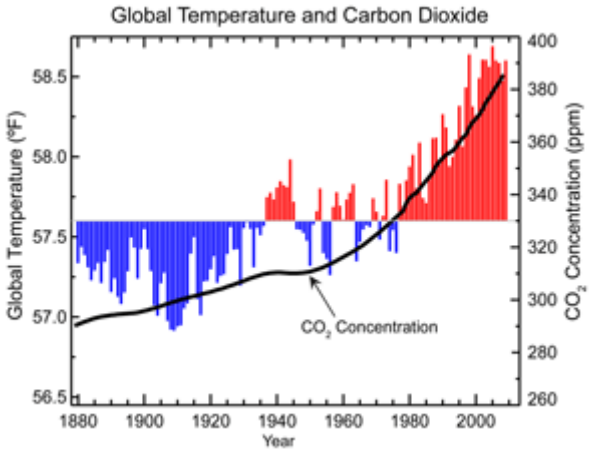

Fig. 1: Global annual average temperature measured over land and oceans. Red bars indicate temperatures above and blue bars indicate temperatures below average temperature between1901-2000 [68].

This correlation is described by the greenhouse effect. The energy coming from the sun, as received by earth, consists of ultraviolet, visible, and near-infrared radiation. In average, around 26% of this incoming radiation is reflected to space and 19% are absorbed by the atmosphere and clouds. But the major part passes through the atmosphere and is absorbed by the earth's surface, which is colder than the photosphere incoming from the sun. As a consequence, thermal energy radiated by earth's surface has a longer wavelength then the before absorbed radiation (Wien´s displacement law). Most of this radiation, now in the wavelength of infrared light (IR), is than absorbed by molecules with an existing or inducible dipole. This absorption is expressed by increased vibrational molecule motions and subsequent collisions, what leads to a transfer of the energy to surrounding molecules [3]. The result is an increase of the average thermal energy and thus a raise of temperature. In principle, all molecules with more than two atoms can be IR absorbers. In the atmosphere, however, are four major gases contributing to the greenhouse gas effect. Water vapour is contributing 36-72%, CO_2 9-26%, CH_4 4-9% and Ozone 3-7% [4]. It has to be noted that the contribution spread is caused by the varying water vapour amount at different locations and time frames.

The anthropogenic contribution to the greenhouse effect is mainly caused by activities which are leading to an increase of atmospheric CO_2. Such activities are predominantly the burning of fossil fuels for industry and mobility and agriculture productions [5–7]. In addition, the greenhouse effect is further amplified by an ice-albedo feedback and the water vapour feedback.[1] It is a scientific and extensive political consensus that climate change is unequivocal and that human activities are almost certainly the main cause of the warming in the past decades [8–10].

Many climate change impacts are already observable on the environment. Glaciers are retreating, the loss of sea ice, melting of ice sheets, the thawing of permafrost soil and more intense heat waves are only some effects [11–13]. The temperature rise causes also a shift in the timing of seasonal events of animals and plants [14]. Although climate change is only at

[1] The ice-albedo feedback is a process where the albedo of ice and snow is reduced due to its melting as a consequence of increased temperature. A reduction of ice reduces the surface albedo and hence, more radiation is absorbed by liquid water what leads to more warming [66]. Another positive occurring feedback is the water-vapour feedback. Hereby, the maximum content of water vapour in the air is strongly depending on temperature. Hence, a temperature increase allows also a higher saturation of water vapour in the air and therefore a further amplification of the greenhouse effect [67].

the beginning of its projected trajectory, there is ample evidence of its effects. Impacts are already clearly visible in ecological and geological aspects.

In this context, the need of a change has been acknowledged by almost all countries in the world. A first international treaty was made 1997 by the Kyoto Protocol. But the enforceability of its binding character remains arguable. The first comprehensive climate agreement was made very recently in Paris. "*The Paris Agreement on climate change, which entered into force in November 2016, brings together countries representing almost all of the world's greenhouse-gas emissions and energy use: it represents a strong signal of the determination of governments around the world to reduce emissions by accelerating the transition to a cleaner and more efficient energy system"* [15]. In Paris, 195 countries agreed to enhance the implementation of the United Nations Framework Convention on Climate Change (UNFCCC). The aim of this particular agreement is to hold the increase of the global average temperature below 2 °C above pre-industrial levels. In addition, pursuing efforts are made to limit the temperature increase to 1.5 °C above pre-industrial levels, recognizing that this would significantly reduce the risks and impacts of climate change. Furthermore, the ability to resist adverse impacts of the climate change must be increased in a way that does not threaten the food production. And last but not least, finance flows must be made consistent with a pathway towards low greenhouse gas emissions and climate-resilient development. In this context, incentives must be set to phase out fossil fuel investments [16].

Although the agreement is called formally binding, obligations are set by the individual state for itself and are sometimes depending on the interpretation of each provision. But the major part of critics concerns about the lack of enforcement mechanism. Hence, the binding character of the agreement remains a point of law [17,18]. On the other hand, this circumstance was crucial for the agreements success. A legal bindingness could discourage states to participate or to make less ambitious commitments [18].

As mentioned above, major points of climate change mitigation is the switchover to non-fossil energy carriers and the transition to a more efficient energy system. The implementation of fuel cells is a possible way to address both of this challenges. Fuel cells offer a significant advantage over traditional heat engines, because they are high efficient energy converters, while causing less emissions. As shown in the illustration below, a power generation from heat

engines allows ideal overall efficiency from about 45%. Fuel cells enable a conversion of chemical-bound energy directly into electric energy. Unlike heat engines, fuel cells are not bound to the limitations of the Carnot efficiency and further conversion steps to produce electricity [19].

As seen below, a fuel cell system has the potential to outperform a heat engine at lower and middle temperatures in theoretic efficiency aspects.

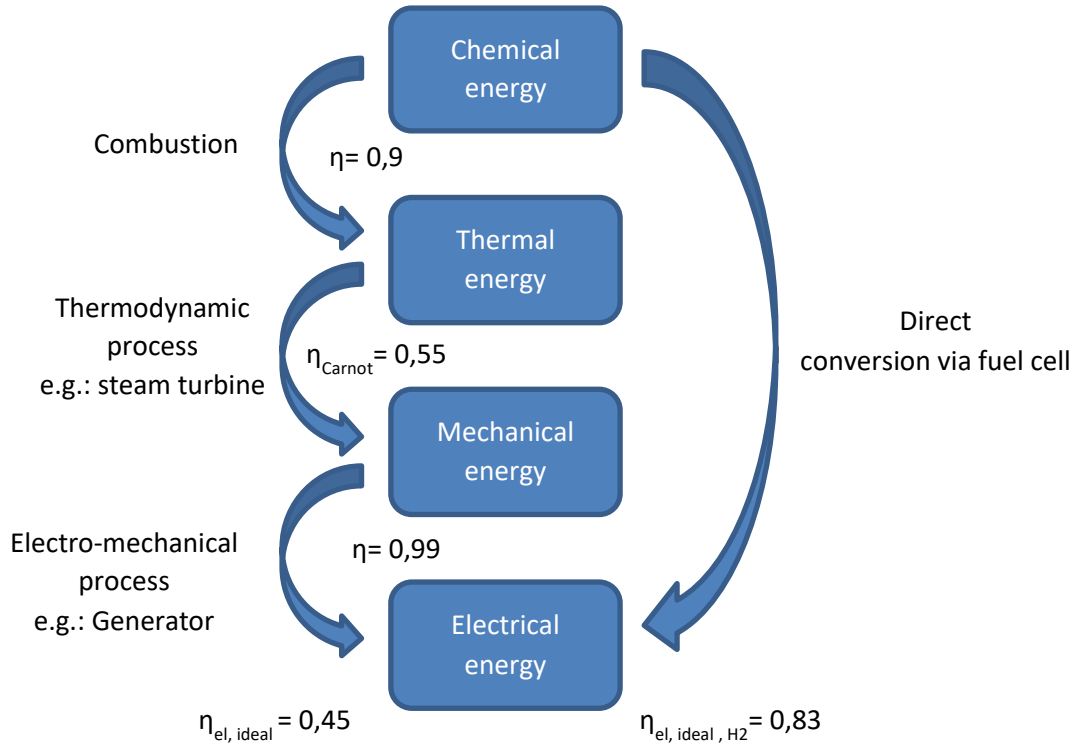

Fig. 2: Process comparison of a heat machine and a fuel cell system

In the view of a sustainable and environmental friendly technology, a renewable fuel production is as crucial as its effective use. Solar and Wind power are beneficial and commercial viable options which meet this criteria. But the power output of these technologies underlies natural fluctuations and cannot be timed. This can cause peak loads and stress for the power grid. A potential solution for this problem might be the usage of surplus power for the generation of hydrogen via electrolysis. The resulting energy carrier can be stored, transported and reconverted to electric energy by a fuel cell in a large scale.

Ethanol as biofuel can also contribute to a carbon-neutral sustainable energy system. The use of ethanol as fuel appears to be beneficial, regarding the logistical and environmental advantages of a liquid hydrogen carrier, which can be obtained by biomass [20]. The high specific

energy (7.41 kWh/kg), which is within the range of fossil fuels, (seen in the following diagram) and its low toxicity makes bioethanol save to store and easy to transport at ambient temperatures and pressures [21].

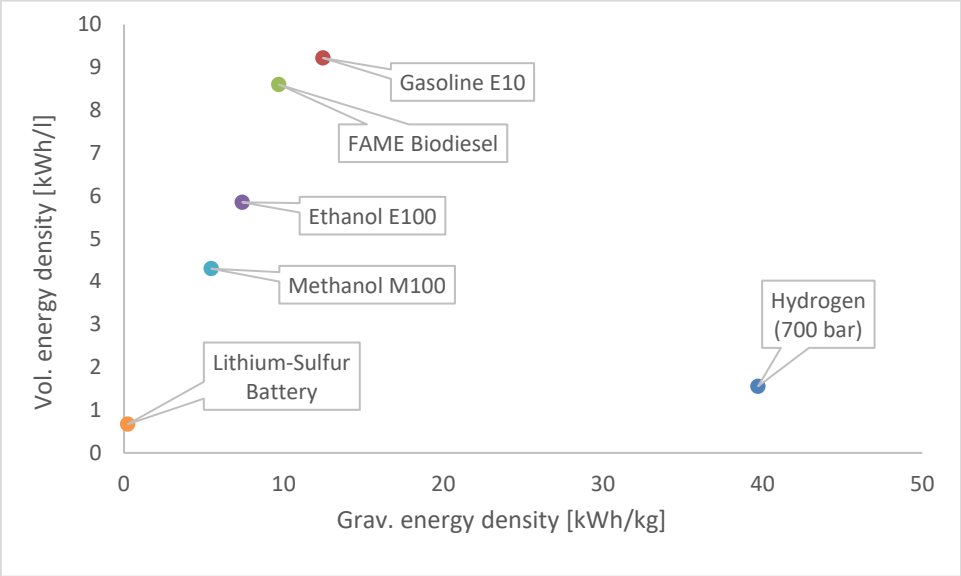

Fig. 3: Specific lower heating values and energies of selected energy carriers [21,69–71]

Ethanol can be fed to direct ethanol fuel cells (DEFC) to produce electrical energy. During the theoretical electro oxidation of ethanol, ideally CO_2, water and heat is released. The save and easy handling makes ethanol a good fuel candidate for mobile and portable applications. It has also a much higher specific energy density than Lithium batteries, which are now the dominant technology in this field of applications. In the future, increasing power demands might surpass the capacity of secondary batteries what might give direct alcohol fuel cells the potential to replace them [22].

In addition, bioethanol is readily available and already produced in a large scale. It is the most common biofuel worldwide [20]. 2016 were globally 83 billion liters of ethanol fuel produced and the production amounts have been strongly increasing within the last years, as seen in Fig. 4 [23] (next page). Most of the producing states are ambitious for a further production increase to gain autonomy from energy imports and to reduce greenhouse gas emissions. The European council for example, sets a mandatory target share of biofuels in transport sector. 10% of minimum fuel additive should be achieved by all Member States by 2020 [24].

For a sustainable reduction of greenhouse gas emissions, it is essential that ethanol, like all biofuels, is produced in a way that does not impair the environmental or social sustainability.

Currently and in the past, forest areas, especially in Brazil, Indonesia and Malaysia, were extensively slashed and burned to plant energy crops. In many cases, the plantation site remained degraded after the cultivation and is abandoned. This land use change leads to a clear increase of net greenhouse gas emission and a reduction of high value land [25,26]. Another important issue, which is needed to be solved in each individual case is the food versus fuel competition. World markets can dictate the decision of what will be planted (food or fuel) or how agriculture products are used (corn, sugarcane for food or fuel). Food and biofuel prices are then linked together. Increasing biofuel demands and prices can lead to a decreased food production and increased food prices [27,28].

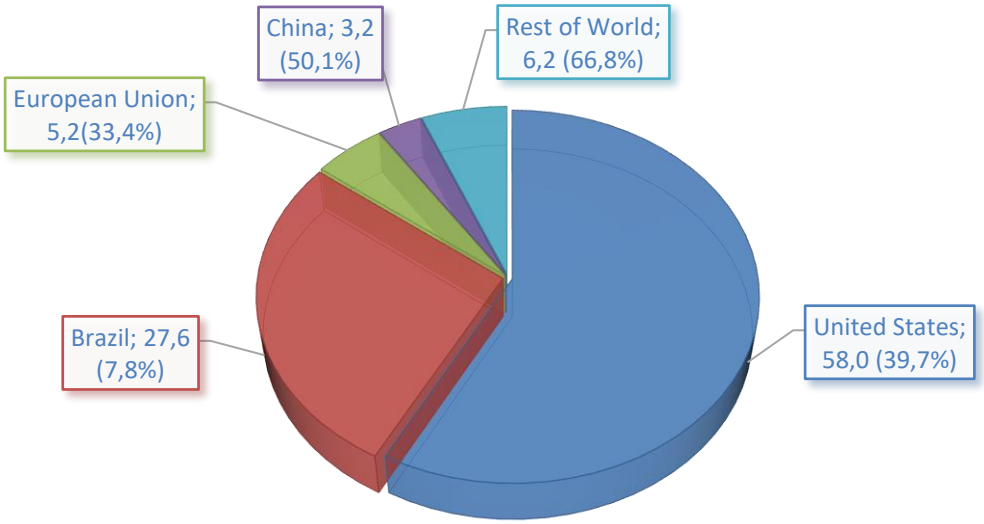

Fig. 4: Ethanol Production in billions of liter and production increase from 2009 to 2016 [23].

To overcome these issues, first comprehensive restrictions have been made by individual states. In this context the EU has set sustainability criteria for their support of biofuels and bioliqiuds to ensure real carbon savings while protecting biodiversity. In 2017, EU supported biofuel productions must achieve at least 50% greenhouse gas saving in comparison to fossil fuel, including the cultivation, processing and transport of the fuel. In EU legislation, biofuels cannot be produced from raw materials obtained from land with high biodiversity (e.g: wetlands or forests). Biofuels cannot be grown on previous high carbon stock land such as wetlands or forests [29].

Biofuels like ethanol can contribute its part to achieve climate goals in a sustainable way, if they are produced and used in a proper and regulated way. Nowadays, as mentioned, ethanol-biofuel is already produced in large-scale and used in combustion engines for mobility. A usage

in fuel cells has the future potential to reach a more efficient energy conversion and to enhance the field of ethanol application. Due to the high energy density and low toxicity of the fuel, as well as the good scalability of fuel cells, an implementation as power supply for portable devices would be beneficial.

2 Theory

2.1 Fuel cell fundamentals

Fuel cells are galvanic cells, which convert the chemical bound energy directly into electrical energy and heat. But in contrast to batteries or accumulators, the fuel is continuously supplied by an external reservoir, similar to combustion engines. The occurring chemical overall reaction is split into two half reactions. At the anode surface, fuel is oxidized. Generated electrons are drawn through an external circuit to the cathode to produce electricity. Thereby, the electrons are “consumed” by reducing the oxidizing agent, which is usually air or pure oxygen. This reaction is called oxygen reduction reaction (ORR). The electric circuit is closed by the ion conductive electrolyte, which plays a key role in the cell design. It can be solid or liquid and proton or anion conductive, which means that the reaction takes place in an acidic or alkaline environment. The Figure below shows the working principle of a polymer electrolyte membrane (PEM) fuel cell with proton exchange.

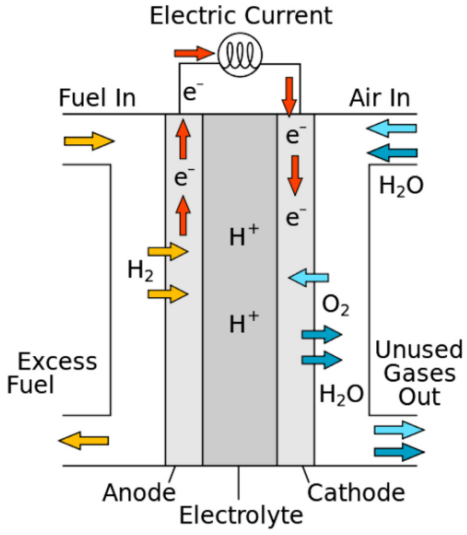

Fig. 5: Schematic of a proton exchange fuel cell membrane [36]

Many varieties of fuel cell types have been developed, concerning fuel, electrolyte or operating conditions. In General, fuel cells are classified by the type of electrolyte and fuel. As mentioned before, the main advantage of fuel cells over heat engines is the bypassing of a conventional combustion and therefore the independence of the Carnot efficiency. In the following this subject is treated in detail by an explanation of the concerned efficiencies.

The Carnot efficiency is defined by the ratio of the energy which is converted to work in the system W and the energy in the form of heat, which is put into the system Q_H. It is calculated by the difference between the working fluid temperature T_H (at the inlet) and the "cooled" off, outlet temperature of the passed out media T_C, divided by the working temperature:

$$\eta_C = \frac{W}{Q_H} = \frac{T_H - T_C}{T_H} = 1 - \frac{T_C}{T_H} \qquad \text{(Eq. 1)}$$

As seen by the equation above, limitations are given by the operating temperatures T_H and T_C of the engine. Increased working temperatures are leading to increased efficiencies. But the working temperature is limited by the temperature resistance of applied materials, while the exiting temperature is limited by the environmental temperature.

However, the thermodynamic efficiency of fuel cells is defined as the amount of the useful energy (change in Gibbs free energy, ΔG_R) relative to the change in stored chemical energy (which is expressed by the reaction enthalpy change, ΔH_R). Under reversible conditions, the following expression applies for the thermodynamic efficiency of fuel cells:

$$\eta_t = \frac{\Delta G_R}{\Delta H_R} = \frac{\Delta H_R - T\Delta S_R}{\Delta H_R} = 1 - \frac{T\Delta S_R}{\Delta H_R} \qquad \text{(Eq. 2)}$$

Limitations in this context are given by the operating temperature. An increased temperature leads to decreased efficiency. The opposed temperature-efficiency behavior of hydrogen and ethanol using fuel cells and heat engines with a lower operating temperature of 127° C is illustrated in Fig. 6. Thereby, the temperature dependencies of the enthalpy and entropy were neglected.

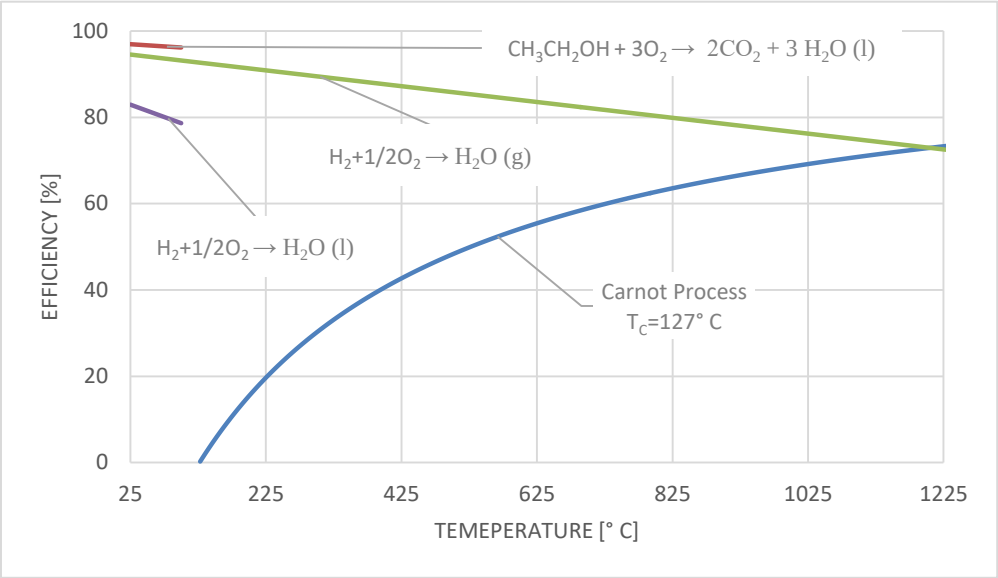

Fig. 6: Comparison of the efficiency of an ethanol and hydrogen fuel cell as well as the Carnot process [72,73]

In general, there are at least three additional efficiencies, besides the thermodynamic efficiency, necessary, to determine the overall energy-conversion efficiency of a fuel cell system [30,31]. Thereby, the overall efficiency is calculated by the multiplication of the thermodynamic efficiency η_t, the voltage efficiency η_E, the faradaic efficiency η_F and the efficiency of additional needed process technologies η_{Sys} (like pumps, humidifier, etc.):

$$\eta_{FC} = \eta_t * \eta_E * \eta_F * \eta_{Sys} \qquad \text{(Eq. 3)}$$

The voltage efficiency η_E describes the occurring overpotential losses. It is the ratio between the operating cell potential E_{Cell} and the reversible cell voltage E_0:

$$\eta_E = \frac{E_{Cell}}{E_0} \qquad \text{(Eq. 4)}$$

This overpotential, which is the differential amount between E_{cell} and E_0, is composed of activation losses, ohmic overpotentials and concentration losses. Activation losses are dominating at low currents. They represent the activation energy to transfer an electron to the electrolyte or vice versa. Ohmic overpotentials are formed by the internal resistance of involved electrical conducting devices (e.g.: electrodes, electrolyte). At high currents, concentration losses are outweighing other overpotentials which are occurring when charge carriers cannot diffuse fast enough to the electrode surface. As a consequence, reaction reactants are depleting at the electrode surface what limits the cell performance. This is mainly controlled by the diffusion coefficient of the reactants and the electrode surface structure. Another important dimension

is the above mentioned reversible standard potential E_0. It depends on the free reaction enthalpy ΔG^0, the transferred electrons and the faradaic constant F:

$$E_0 = \frac{-\Delta G^0}{nF} \qquad \text{(Eq. 5)}$$

The faradaic efficiency η_F takes the oxidation degree into account. It is affected by side reactions which prevent a release of electrons during the oxidations. The determination of η_F can be done by the division of the actual released electrons (n_a) and the maximum possible number of transferred electrons (n_t):

$$\eta_F = \frac{n_a}{n_t} \qquad \text{(Eq. 6)}$$

The table below lists some of the common fuel cell types with their electrolyte, working temperature and overall efficiencies.

Table 1: Selected fuel cell types with main properties and their efficiencies.

Fuel cell type	Common Electrolyte	Operating temperature [° C]	Efficiency
Polymer Electrolyte Membrane (PEM)	Perfluoro sulfonic acid	50-100	45-50, [32–34]
Alkaline (AFC)	Aqueous solution of potassium hydroxide	90-100	50, [33,34]
Solid Oxide (SOFC)	Yttria stabilized zirconia	500-1000	50-60, [33,34]
Direct Methanol (DMFC)	Polymer membrane (ionomer)	20-60	20-25, [34]
Direct Ethanol (DEFC)	Polymer membrane (ionomer)	25-80	<12, [35]

2.2 The direct ethanol fuel cell (DEFC)

Direct ethanol fuel cell (DEFC) technologies have been an increasing research topic within the last years. Already established direct alcohol fuel cells are using methanol as energy carrier. In contrast to methanol, the use of ethanol would not cause safety issues due to its lower toxicity. However, ethanol contains a carbon bond which is needed to be broken to reach the maximum of the theoretic cell efficiency [36]. The full conversion of ethanol would lead to the formation of CO_2, as seen in the reaction equation below.

$$CH_3CH_2OH + 3O_2 \rightarrow 2CO_2 + 3H_2O \qquad \text{(Eq. 7)}$$

Up to the present, it is a main DEFC research topic to find suitable catalysts which achieve a high conversion rate of ethanol to CO_2. By the use of state of the art catalysts, the electrooxidation of ethanol is a complex multistep reaction which leads mainly to acetic acid and acetaldehyde and only small amounts of CO_2 [20,30,36]:

$$CH_3CH_2OH + \frac{3}{4}O_2 \rightarrow \frac{1}{2}CH_3COOH + \frac{1}{2}CH_3CHO + H_2O \qquad \text{(Eq. 8)}$$

While the complete oxidation of ethanol yield 12 electrons, the formation of acetaldehyde and acetic acid releases 2 and accordingly 4 electrons. This significantly lowers the faradaic efficiency. An ethanol oxidation with the end product of acetaldehyde and acetic acid in the ratio of 1:1 would lead to an ideal faradaic efficiency of just roughly 25 %. This low efficiency and sluggish anode kinetics are the biggest challenge which prevents the DEFC from commercialization [20,30,36].

The ethanol oxidation and ion transfer can occur in an acidic or alkaline environment [22,37]. The half-cell reaction in an alkaline environment for a four electron oxygen reduction reaction and a full ethanol oxidation are shown in Eq. 9-12.

Anode: $CH_3CH_2OH + 12OH^- \rightarrow 2CO_2 + 9H_2O + 12\,e^-$ (Eq. 9)

Cathode $3O_2 + 6H_2O + 12\,e^- \rightarrow 12OH^-$ (Eq. 10)

In acidic environment:

Anode: $CH_3CH_2OH + 3H_2O \rightarrow 12H^+ + 2CO_2 + 12\,e^-$ (Eq. 11)

Cathode: $3O_2 + 12H^+ + 12\,e^- \rightarrow 6H_2O$ (Eq. 12)

The use of alkaline electrolytes enhances the number of catalyst prospects because it is less corrosive than acidic environments and allows the use of non-precious metal catalysts. First developed alkaline fuel cells were using dissolved potassium hydroxide as electrolyte which is inexpensive, has high ion conductivity and allows simple thermal management to remove the reaction heat from the system [36]. Another main advantage of using high pH electrolytes are the increased oxidation kinetics. The media provides additional OH^- ions on the catalyst surface, which are required in general ethanol oxidation mechanism and thus enhances the oxidation reaction [36]. On the other hand, a liquid alkaline electrolyte is difficult to handle practical applications. A major issue which prevented the hydrogen alkaline fuel cell with liquid electrolytes from commercialization is the CO_2 poisoning by the usage of ambient air as oxidants. CO_2 in contact with the electrolyte leads to the formation of carbonate crystals, which blocks the diffusion paths and mechanically destroys the electrode layer [36]. Additionally, DEFCs with a liquid alkaline electrolyte face another problem. Acetic acid, which can be a side product during the ethanol oxidation, neutralizes the hydroxide anions what leads to reduced ion conductivity [36].

To avoid these problems, recent alkaline fuel cell research is mainly focused on using polymer alkaline membranes. However, the development of these membranes is still limited by low ion conductivities. Additionally the use of these membranes requires wetting with KOH and water to achieve satisfying conductivities [30].

Another approach is the use of proton conducting, acidic membranes, which benefit from the advanced development of Nafion-based polymer electrolyte membranes (PEM). The acidic environment prevents the precipitation of most salts which is a decisive advantage. On the contrary, only platinum based catalysts showed in this media high performances which are expensive, rare and prone to CO poisonings [36]. An et al. state that the cost per kilowatt hour of acidic DEFC are about 20 times higher than for PEMFCs due to the higher amount of required platinum and Nafion [30].

2.3 The oxygen reduction reaction

The oxygen reduction reaction (ORR) at the cathode is the fundamental reaction of this work. ORR equations in alkaline and acidic media are listed above (Eq. 9-12). In acidic media, the ORR is the kinetically limiting reaction and gains therefore much scientific attention. On the contrary, the ORR in alkaline media is much faster [37–39].

However, there is no scientific consensus on the exact ORR mechanism due to the difficult determination of surface intermediates during the reaction. It includes several reaction steps and a wide choice of reaction pathways [37]. But it is general accepted, that overall, the ORR occurs either through a direct four electron pathway (Eq.10) or an indirect two electron pathway (Eq. 13). These two pathways can occur simultaneously while competing with each other at different rate constants. As shown in the illustration below (Fig. 7), the overall direct four-electron mechanism skips intermediates and is known to be the more efficient pathway [37–40].

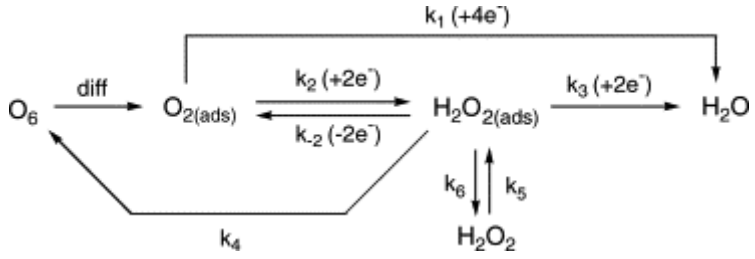

Fig. 7: General ORR reaction scheme [74]

The two-electron mechanism involves hydrogen peroxide (H_2O_2) intermediates in ad- and desorbed form. This pathway does not only have the potential to reduce the number of transferred electrons (and therefore the faradaic efficiency), it also produces a chemical problematic compound which can further be converted into a harmful radical species [39,41,42]. In alkaline media, the formation (Eq. 13) of superoxides and peroxides and in redox processes dominates.

$$O_2 + H_2O + 2\,e^- \rightarrow OH^- + HO_2^- \qquad \text{(Eq. 13)}$$

The reaction of the two electron pathway can stop at the, in alkaline relatively stable solvated, HO_2^- ion. But it may undergo a further disproportionation (Eq. 14) or reduction reaction (Eq. 15) which leads overall to a “2+2-electron” pathway:

$$2HO_2^- \leftrightarrow O_2 + 2OH^- \qquad \text{(Eq. 14)}$$

$$HO_2^- + H_2O + 2e^- \rightarrow 3OH^- \qquad \text{(Eq. 15)}$$

At the present, platinum cathode catalysts are usually applied in both alkaline and acidic electrolytes, since they have shown high performances [36]. On the other hand, platinum is a rare, precious metal with the ability to catalyze both, the fuel oxidation and oxygen reduction reaction. For this reason, occurring fuel crossovers cause the formation of mixed potentials and a reduction of cell performance. It is beneficial to replace platinum with inexpensive earth-abundant materials, for promoting the ORR. In this case, nano-structured metal oxides have gained recently much attention [37–40,43,44]. They are easy to prepare, have a promising activity and a good stability in alkaline environment. By use of co-catalysts and perovskite-type nanostructures, disadvantages like poor electrical conductivity and weak oxygen sorption on the surface has to be handled [38].

Perovskites, which are used to catalyze the ORR exhibit the formula ABO_3 (A=La, Ca, Sr, or Ba, and B=Ni, Co, Fe, Mn, or Cr). The structure of the unit cell is seen in Fig. 8 [45]. They consist of an octahedral with corner shared oxygen “O” and “B” cations in the center. The “A” elements occupy the corner of the unit cell and are primarily contributing to the stability of the overall structure.

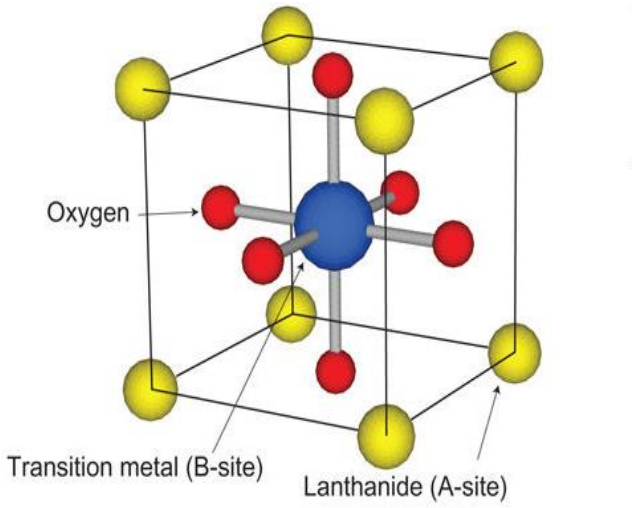

Fig. 8: Unit cell of Perovskite structure [45]

Sunvtivich et al assume that the B site materials are largely responsible for the ORR activity by interacting with the surface adsorbed oxygen species. This interaction has to be neither too

strong nor too weak to achieve maximum activity [45]. Overall, perovskites have a flexible and robust structure with a variable conductivity [37]. The catalytic activity can further be tailored by the addition of a third cation, which partially substitutes the A and B sites in the perovskite structure to from AA´BB`O_3 [38,45].

As mentioned above, the exact reaction mechanism remains unconfirmed. Although, it is known that some of the elementary steps involve intermediates, what leads to a large variety of reaction pathways [37]. Thereby, the known reaction at transition metal oxide surfaces is different to the ORR of precious metals. Suntivich et al. provide a proposed mechanism and the schematic reaction pathway, seen in Fig. 9a. The transition metal oxides coordinates with oxygen atoms from H_2O to achieve full oxygen coordination and to regenerate surface hydroxide substituents. The remaining hydrogen atoms are distributed over the catalyst surface and charge compensation takes place by the reduction of metal surface cations (step 4). The next step (step 1) is the displacement of surface hydroxide by O_2 molecules, what is assumed to be the rate determining step. Further, surface peroxides (step 2) and oxides (step3) are formed. Suntivich et al assume that the rate determining step, and therefore the ORR activity, is primarily correlating with the occupation of the σ^* -orbital (e_g) of the B site transition metal. If the orbital is filled with more than one electron (right branches of Fig 9b), the hydroxide displacement (step 1) does not receive sufficient energy what limits the ORR kinetics. On the other hand, if the electron filling (e_g) is less than one electron, the B-O^2 state is not effectual destabilized which hinders the regeneration of the surface hydroxides (step 4) [45]. According to these findings, an electron filling of one provides maximum activity. (e.g.: $LaMnO_3$, $LaNiO_3$, and $LaCoO_3$, as seen in Fig. 9b).

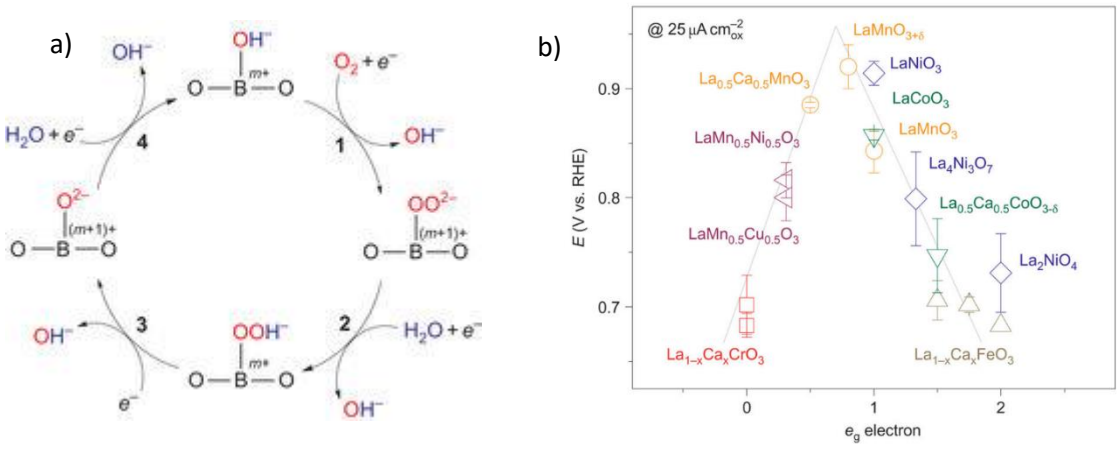

Fig. 9: a) Proposed ORR mechanism of perovskite catalysts, b) Potentials at 25 µA/cm²$_{ox}$ of different perovkites and relationship with d-electron number [45]

2.4 ORR rotating disk electrode analysis

Rotating disk electrode measurements are the ex-situ method of choice to investigate the oxygen reduction reaction. It is a fast, inexpensive and reproducible potentiodynamic method which requires only small amounts of catalysts [46].

The measured currents between working and counter electrode give information about redox reactions at the catalyst surface. The measurements in this study were done by a three-electrode set up in potassium hydroxide electrolyte. The third electrode is used as reference electrode and allows a current independent measurement and controlling of the applied potential. For the analysis, the catalyst is applied as a thin-film on a rotating disk electrode (working electrode). In the following, a potential is cycled up and down in a given range. The resulting cyclic voltammogram (the plot of applied potential versus measured current) represents oxidation and reduction processes at the electrode [47]. The base cyclic voltammogram shows the reversible redox reactions of the catalyst, recorded in the absence of any other reactants. Thereby, the amount of measured current increases with rising oxidation reactions, what results in characteristic peaks. The reverse sweep exhibits the complementary, reduction, peak [47]. The introduction of oxygen leads to an investigation of the catalyst activity. Hereby, the electroactive reactant is continuously supplied by diffusion to the catalyst layer. As a consequence, the reduction current increases until a maximum, caused by diffusion limitations, is reached. Therefore, the resulting cyclic voltammogram appears as a sigmoidal curve, without distinct peaks [47]. Measurements at various electrode rotation speeds allow conclusions about the mass transport limitation and reaction kinetic properties of the catalyst. This relationship is modelled by the Koutecky-Levich analysis by using the well-known mass transport correction as shown in Eq. 16.

$$\frac{1}{i_{measured}} = \frac{1}{i_k} + \frac{1}{i_D} = \frac{1}{n\,F\,A\,k_h\,C_b} + \frac{1}{0.62\,n\,FA\,D^{2/3}\,\nu^{-1/6}\omega^{1/2}\,C_b} \qquad \text{(Eq. 16)}$$

This equation describes the correlation of the measured oxygen reduction current density ($i_{measured}$), the activation controlled kinetic current density (i_K) and the diffusion limiting current density (i_D).

The analysis is done by plotting the reciprocal $i_{measured}$ against $\omega^{-1/2}$. For each evaluated potential, a linear correlation should be achieved. From the slope of this line, the numbers of transferred electrons (n) can be derived by the knowledge of all other relevant parameters. The intercept describes the kinetic limitations and allows the determination of the heterogeneous rate constant k_h.

The table below presents all required parameters for the Koutecky-Levich analysis in 1 M KOH electrolyte as stated by Qiao et at [48].

Table 2: All used parameters for the Koutecky-Levich analysis in 1 M KOH electrolyte [48].

F	Faraday constant	96485	As mol^{-1}
A	Area of electrode	0.196	cm^2
D	Diffusion coefficient	$1.8*10^{-5}$	$cm^2\ s^{-1}$
ω	Rotation rate	42-168	rad s^{-1}
v	Kinematic viscosity	0.01	$cm^2\ s^{-1}$
C_b	Bulk concentration	$7.8*10^{-7}$	mol cm^{-3}

2.5 Electrode design

The cathode-electrode design, which was used in this work, is similar to AFC electrodes for liquid electrolytes. The principle structure consists of an active layer, a gas diffusion layer and a backing material, as seen in the figure below. The active layer is in direct contact to the electrolyte and contains the catalyst, carbon to improve the conductivity and surface area and PTFE. The PTFE binder is an essential component in the electrode assembly since it is required for the catalyst immobilization and to achieve a porous structure which is necessary for the stable establishment of three phase boundaries. Thereby, the binder amount and respectively, the degree of hydrophobicity and porosity of the electrode must be balanced to avoid excessive wetting and to maintain sufficient electrode stability as well as electrolyte interaction [40,49,50]. The gas diffusion layer contains carbon and PTFE. This layer is semipermeable which prevents the liquid electrolyte from leaking through the electrode while supplying the active layer with reactant gas. This is achieved by increased hydrophobicity in this layer due to higher PTFE concentrations (which are usually between 25-60%) [40]. The backing material is used as current collector and to improve the mechanical stability. It should have a high corrosion resistance and permeability for the reactant gas. Common materials are metal screens, foams or meshes (usually made of Nickel).

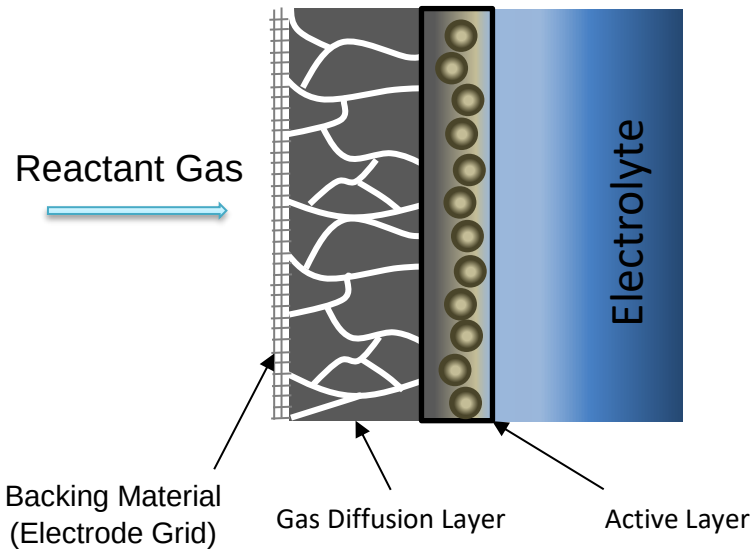

Fig. 10: Schematic of a general gas diffusion electrode for liquid electrolytes

2.6 KOH concentration and temperature

The concentration of the OH^- anions does not only affect anode reaction kinetics, it also has a major influence on the internal cell resistance and diffusion abilities of reactants. The conductivity increases with rising charge carriers. This relationship is linear for low and high KOH concentrations. At a certain point, the ions begin to hinder themselves in mobility what leads to increased resistance. This flattens the resulting curve until a maximum is reached. This maximum is linked to the ion mobility and therefore to the electrolytes temperature, as seen in Fig. 11 [51,52].

As show in the figure above, the maximum conductivity at room temperature is given for a 6.2 molar KOH solution. In practical DEFC applications with a liquid electrolyte, the optimum KOH concentration is additionally limited by a corresponding ethanol concentration [53,54]. Wang et al. achieved in their study (with Pd catalysts) a maximum power density by using electrolytes containing 4 M KOH and 4 M EtOH. A further KOH concentration increase led to decrease of maximum power density [54].

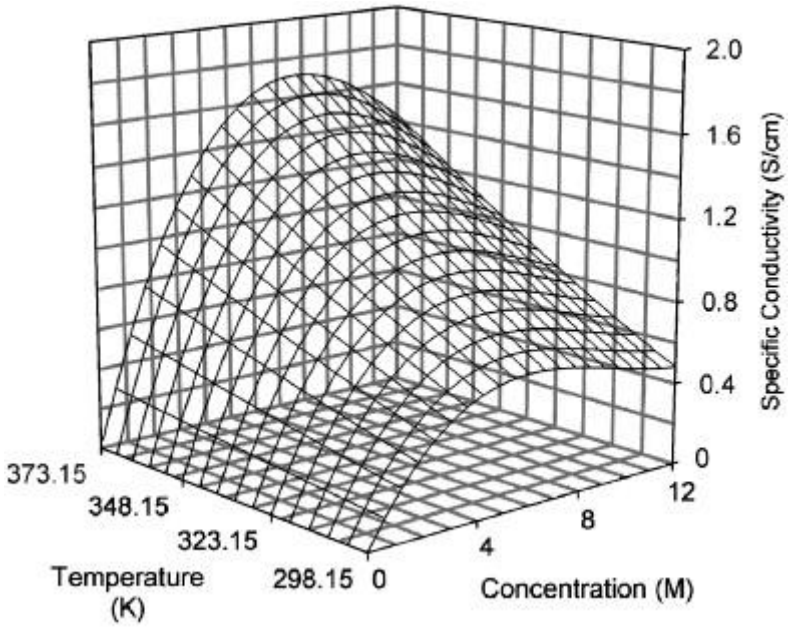

Fig. 11: Concentration-conductivity, relationship of KOH electrolyte at various temperatures [75].

2.7 Degradation effects

One main drawback, which prevents a further commercialization of AFCs is the reduced lifetime in comparison to PEMFCs. Lifetimes of around 5,000 hours have been reported by Geeter et al. for a AFC stack with an air feed and CO_2 scrubber [55]. By the use of pure oxygen, a module produced by Siemens achieved 20,000 hours lifetime with Ag-cathodes [40]. These lifetimes, however, are rather low in comparison to other fuel cell technologies, compared in the table below.

Table 3: Comparison of fuel cell types by their lifetimes

Fuel cell type	Assumed lifetime [hours]
AFC stack	5-20,000 [40,55]
PAFC stack	40-60,000 [56]
PEMFC stack	20-80,000 [56]
SOFC stack	8-16,0000 [56]

Alkaline direct alcohol fuel cells suffer from similar degradation as AFCs, which reduces the lifetime. In this context are AFC degradation effects discussed at this point. As stated by Cifrain and Kordesch, the main effects caused by the use of a liquid electrolyte, are electrode soaking, corrosion, the mechanical destruction of electrodes by the formation of carbonate crystals and catalyst decomposition [49].

The biggest challenge in AFC-technology is the formation of carbonate crystals generated by CO_2 in the feed gas. The carbonate blocks diffusion paths and active catalyst sides. The precipitations lead to increased resistance and reduced O_2 solubility. In addition, the crystals penetrate through the electrode layer what causes a mechanical damage [40,49] .

Also, plastics like PTFE are stressed by the hot caustic electrolyte and the containing radicals [49]. The radicals are formed by peroxides, which are generated by an incomplete ORR. Also perovskite catalysts can proceed via the peroxide forming, 2+2 electron pathway [57]. These radicals can induce a corrosion of carbon and a radical chain destruction in the PTFE binder what leads to reduced mechanical stability and crack formation [40,49]. A crack formation, for any reason, causes the partially destruction of the electrodes conductivity and hydrophobicity,

what leads to increased resistance and electrode soaking. As consequence, the number of three phase boundaries suffers what induces mass transfer losses [49].

3 Experimental

Two perovskites and a silver-based catalyst were manufactured from nitrate precursors. To analyze the physical properties of the prepared catalysts, scanning electron microscopy (SEM) and X-ray diffraction investigations were performed. Rotating disk measurements were executed (RDE) to investigate the catalysts performances and to compare it with literature data. A series of half-cell experiments were performed, aiming to investigate the influence of the electrolyte concentration, the operating temperature and the partial pressure of oxygen on the cathodes performances in an in-situ environment. In addition, long-term measurements reveal the stability of the cathodes. Fuel-cell experiments were conducted to achieve information about the suitability of the prepared cathodes to operate under working conditions. The degraded electrodes were analyzed using SEM investigations and compared with unused electrodes. Additionally, the morphology change, caused by electrode sintering was investigated. Therefore, a sample of the pre-sintered electrode was also examined with SEM. Fig. 12 summarizes the process flow and the performed measurements.

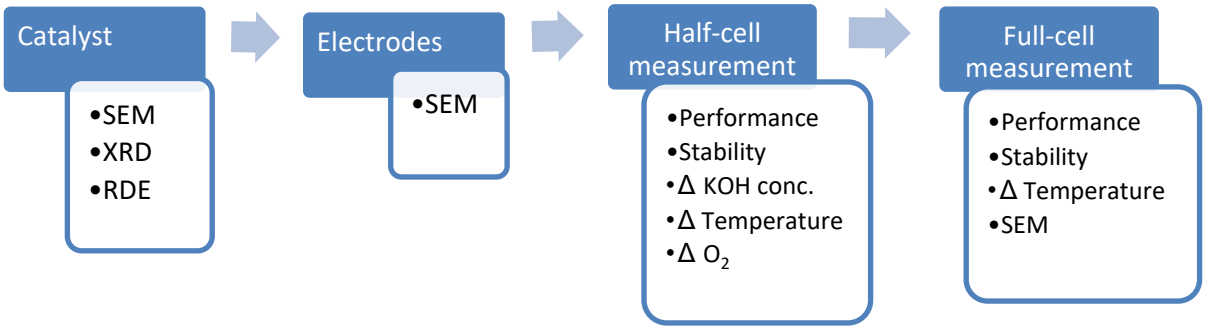

Fig. 12: Process sequence and characterization methods as well as investigated influences of this work

3.1 Preparation of the $AgMn_xO_y$/C catalyst

The catalyst for the cathodes was prepared according to the report from Tang et al. and Wu et al. [58,59]. As carbon powder, Vulcan XC72R and Black Pearls 2000 were used. Therefore, the carbon powders were mixed with 200 ml doubly deionized water (18 MΩ cm) and approximately 20 ml isopropanol for 15min in an ultrasonic bath. After that, $KMnO_4$ and $AgNO_3$ (molar ratio of 1:1) were added and an additional mixing took place for 30 min with an ultrasonic finger. Then, the mixture was concentrated on a heating plate and dried overnight at 50 °C. The

achieved powder was tempered for 2 h at 400 °C in the tube furnace to reduce the manganese in N_2 atmosphere. The final powder was grinded and sieved to a size <45 µm. According to the used literature the achieved composition was approximately 15 % Mn_xO_y and 22 % Ag.

3.2 Preparation of the perovskite catalysts

$La_{0.7}Sr_{0.3}(Fe_{0.2}Co_{0.8})O_3$ and $La_{0.7}Sr_{0.3}MnO_3$ catalysts were prepared according to Tulloch et al. [41]. The preparation method is a sol-gel technique with citric acid (CA) as complexing agent and ethylene glycol (EG) as surfactant. Therefore, the metal-nitrate salts were individual dissolved in a minimum amount of ultrapure water. The solutions were combined and CA was added in the double molar concentration of the metals (CA/metals, 2/1). The mixture was stirred for 1 hour at 80 °C before EG was added dropwise to the solution (in the molar ratio of 1/1 according to CA). The obtained mixture was stirred at 80 °C until the gelation was completed. Fig. 13 shows the $La_{0.7}Sr_{0.3}(Fe_{0.2}Co_{0.8})O_3$ catalyst precursor during the gelation process. The resulting solid mixture was dried at 40° C before calcination. Therefore, the obtained powder was Grinded to smaller pieces, heated up to 250 °C (for 2 hours) and then to 800 °C for 12 hours (heating rate: 10° C/min) under oxygen atmosphere. The resulting material was cooled down and grinded with a ball mill in ethanol for 20 min. A test screening confirmed the resulting particle size of <45 µm.

Fig. 13: Foaming of the Fe-based perovskite catalyst during the gelation process

3.3 Preparation of the gas diffusion layers (GDL)

The GDL consisted of 55 wt.% Acetylene Black and 45 wt.% PTFE. Hence, Acetylene Black (20 g) was mixed with PTFE (16.36 g) and 250 ml Isopropanol/H2O 1:1 (v/v) in a GRINDOMIX GEM 100 (Retsch) for 10 x 5 sec. The obtained slurry was rolled to a thickness of 1.5 mm for the final GDL.

3.4 Preparation of the Cathodes

The electrodes were prepared with various synthesized catalysts and different binder (PTFE) concentrations. One electrode consisted of overall 1.3 g solid matter, including the catalyst, carbon powder and a defined PTFE concentration (15, 20 or 25%). The perovskite electrodes consisted of 60% catalyst and varying PTFE concentrations. The remaining amount was filled with carbon powder (Blackpearls and Vulcan, 1:1). The Ag-based catalyst was already deposited on carbon (Blackpearls or Vulcan). To these electrodes, only PTFE was added. After weighting the substances, Isopropanol/H2O 1:1 (v/v) was added to achieve a slurry, which was rigorous mixed. The slurry was rolled to 1.5 mm layer thickness and combined with the GDL. Both layers were stacked and rolled until the desired catalyst loading was achieved. After that, the combined layers were pressed twice to dry the resulting electrode (5 min at 80 kg/cm² each time). The resulting catalyst loadings were for the perovskite electrodes around 35-50 mg/cm² and for the Ag-based electrodes around 15-20 mg/cm². The layer thicknesses were measured at three points of the electrodes, the average results were between 0.8 and 1.0 mm for every electrode. After stacking it on a 3 cm x 10 cm Ni- mesh, which acts as current collector, the electrodes were sintered for 30 min at 300 °C with a pressure of 120 kg/cm². Finally, the electrodes were pasted into the electrode housing.

3.5 Preparation of the Anodes

The anodes were prepared similarly to the cathodes with the difference that no GDL was used. Commercially available platinum-ruthenium-carbon (40 wt.% Pt, 20 wt.% Ru, 40 wt.% C) was used as catalyst. The final electrodes were composed of 20 wt.% PtRuC catalyst, 25 wt.% PTFE and 55 wt.% additional carbon (Black Pearls and Vulcan, 1:1). These mixtures were

blended with approximately 3 ml Isopropanol/H2O 1:1 (v/v) and stirred until pastes were obtained. The pastes were rolled to a thickness of 1 mm and dry-pressed to achieve electrode layers. The layers were stacked onto a Ni-mesh before sintering. The pressing and sintering were performed as described for the cathodes. The final electrodes were placed in a half-cell housing and had a platinum loading of 2 mg/cm².

3.6 Half-cell measurements

The in situ measurements were conducted by the use of cell designs from the TU GRAZ, using a three electrode set-up. The half-cell includes a housing (with implemented flow field and the connection for a Luggin capillary), the working electrode assembly and a counter electrode (a stainless spatula). As reference electrode a RHE from Gaskatel was used. Fig. 14 illustrates

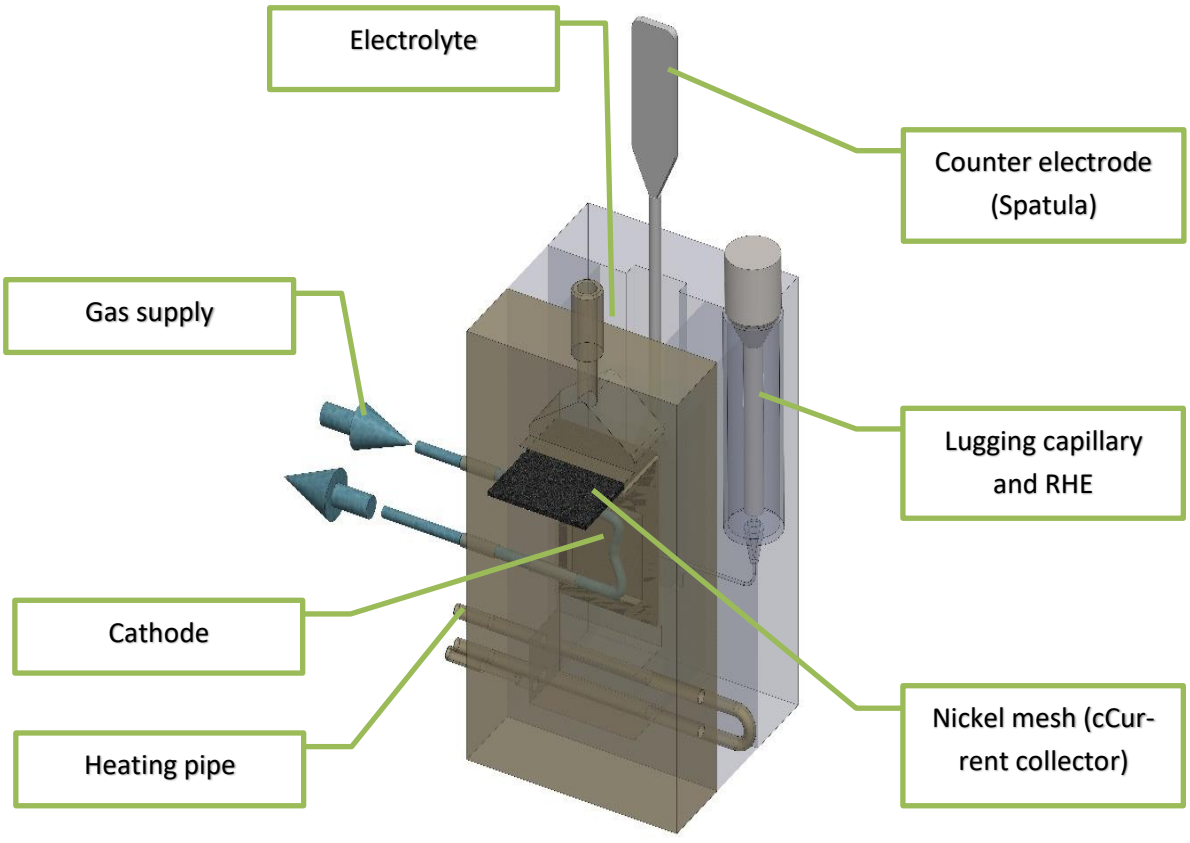

Fig. 14: Half-cell design of the in-situ measurements

the used cell design.

All experiments were performed in 6 M KOH as electrolyte, accept the explicit named measurement series, where 1 M and 3 M KOH were used. If not stated otherwise, the cathode feed

gas was 30 ml/min in case of synthetic air and 6 ml/min for pure oxygen. After connecting the cells to a multichannel cell test system (BaSyTec), polarization curves were recorded potentiostatically with potentials ranging from 0.9 to 0.6 V in 50 mV steps. During long-term operation, the cells were hold at a constant potential of 0.75 V. All measurements were recorded at room temperature accept for the temperature investigation, were the cells were connected to a thermostat to reach a constant cell temperature of approximately 45 °C. During the long-term measurements, the electrolyte/ethanol mixture was overlaid with silicone oil to reduce evaporation.

3.7 Fuel cell measurements

The fuel cell measurements were performed with the perovskite cathodes (20 wt.% PTFE) and PtRuC anodes. Both electrode housings were screwed together, with gaskets including the lugging capillary to form the fuel cell as seen in Fig. 15. In addition, a polypropylene separator was used to avoid short circuits within the cells. During the first measurements, 6 M KOH and 1 M EtOH electrolyte/fuel mixture was pumped through the cells with 3 ml/min. After that, 6 M KOH 2 M EtOH mixture was used to investigate a stability change. As feed gas, approximately 30 ml/min pure oxygen were used. All measurements were performed at room temperature, accept of the explicit named ones at elevated temperatures. In this case, the cells were connected to a thermostat, as performed at the half-cell measurements. The full-cells were connected to the BaSyTec test system in a three electrode set-up. The cathode was acting as working electrode and anode as counter electrode. Additionally, a RHE was used to track the anode potential. The polarization curves were recorded from cell voltages ranging from 0.9 V to 0.1 V. In between of the polarization curve recordings, the cells were operated at constant potentials of 3.5 V.

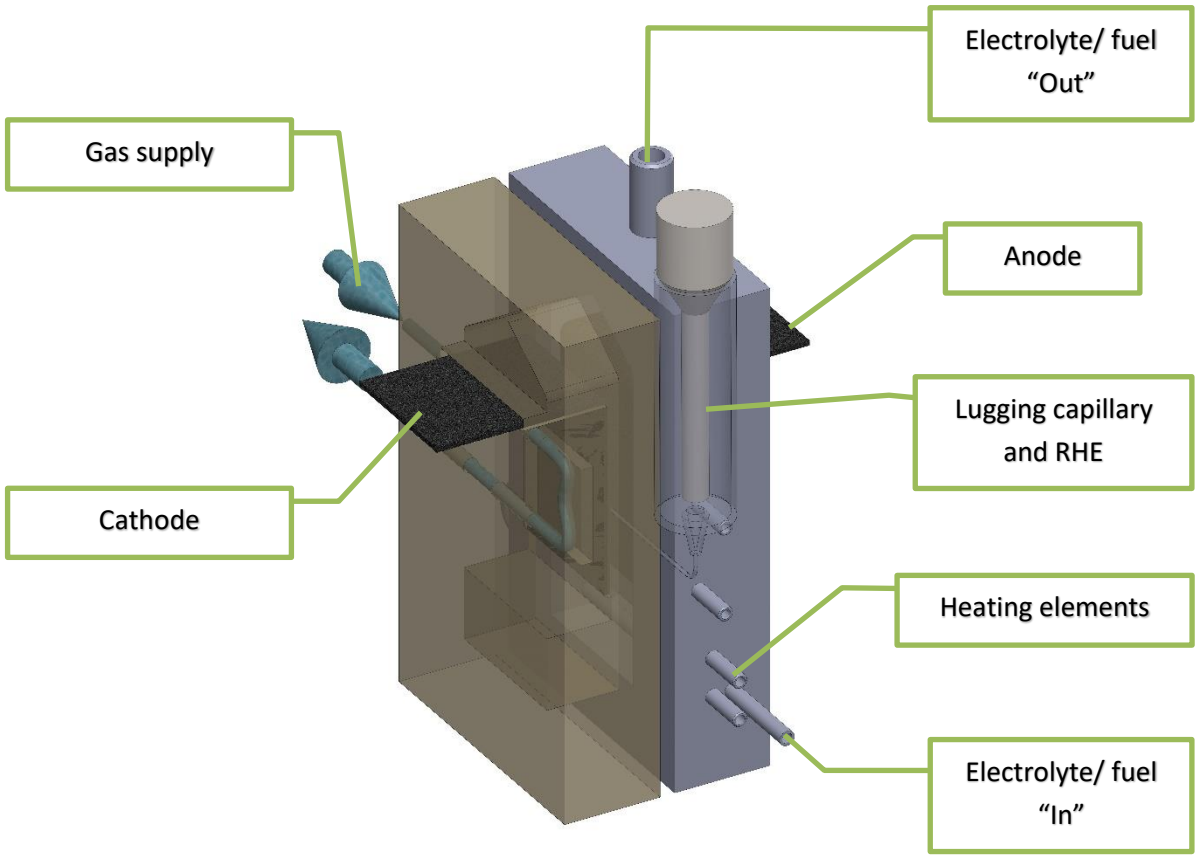

Fig. 15: Full-cell design of the fuel cell measurements

3.8 RDE measurements

The RDE measurements were performed in a 3-electrode set up, using glassy carbon as counter electrode and a RHE as reference electrode. As electrolyte, 50 ml of 1 M KOH solution was heated up to 30° C in a thermostatic three-compartment cell. The electrode preparation, RDE measurement sequence and the performed analysis are described in the following.

3.8.1 Preparation for the RDE measurements

For the measurements, the electrode (0.196 cm²) was coated with the respective catalyst suspension resulting in a loading of 210 µg/cm². 3 ml catalyst suspensions were prepared, whereof 10 µl were taken in case of the perovskites and 17 µl in case of the Ag-based catalyst to coat the electrode surface. Before the coating, the catalyst-suspension mixture was suspended for at least 30 min in a solution of 3 ml Nafion (5 wt.%, from Quintech), ethanol and ultrapure water (Nafion:EtOH:H2O = 2:49:49) using an ultrasonic bath. The suspensions were applied in small portions (2-5 µl) to the electrode surface to achieve a sufficient fixation. After every injection,

the electrode was rotated with 700 rpm for 5min to dry the previous coated layer. After the coating, the electrode was dried at 700 rpm for 30 min.

3.8.2 RDE parameters and measurement sequence

After the preparation of the electrode, the following measurement sequences were executed.

1. 20 cleaning circles at potentials of 0.1 - 0.5 V with 100 mV/s in N_2 atmosphere
2. Recording of 3 base CVs from 0.1 - 1.0 V with 10 mV/sec in N_2
3. Measuring of the internal resistance (iRu)
4. Purging of the electrolyte with O_2 for 20 min
5. Recording of CVs (0.1 – 1.0 V, 10 mV/min) at various rotations in the following order 1600, 1200, 900, 600, 400 rpm.

4 Results and discussion

In the following, the results of the In- and Ex-situ measurements and the physical characterization are presented. Thereby, the influence of the binder and operation conditions were investigated during half-cell In-situ measurements. The measurements were mostly performed at new and unused electrodes to avoid the implication of degradation effects. Stability investigations were also conducted in a half-cell measurement set-up, but under constant operation conditions over a couple of hundred hours. Section 4.3 summarizes and compares the main findings of the half-cell measurements. The fuel cell measurements confirmed the suitability of the perovskite cathodes to operate under practical conditions. The physical characterization via SEM revealed the effect of the sintering and changes due to long time operations on the surface. The XRD-analysis confirmed the successful preparation of the catalyst regarding the phase purity and impurities.

4.1 Influence of binder and operation conditions

As mentioned above, half-cell measurements of the cathodes were performed with varying binder amounts and operation conditions. The results can be found in the following sections.

4.1.1 Influence of the PTFE binder concentration

In order to identify a proper PTFE concentration, electrodes with 15%, 20% and 25% PTFE were prepared and investigated regarding their initial performance in KOH.

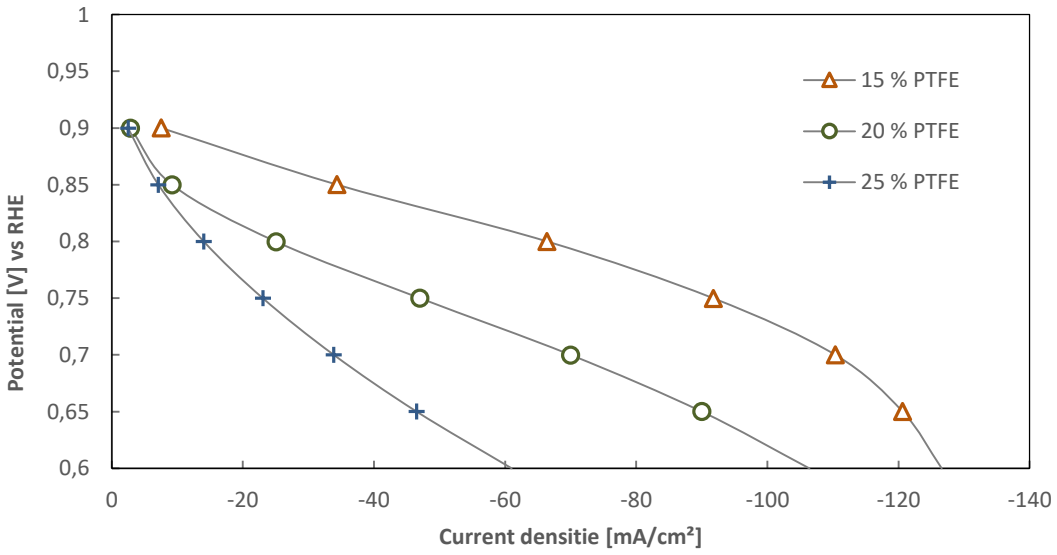

Fig. 16: $La_{0.7}Sr_{0.3}MnO_3$ perovskite polarization curves with different PTFE amounts

The results of the $La_{0.7}Sr_{0.3}MnO_3$ catalyst are shown in Fig. 16. It can be seen, that the electrode with the lowest PTFE concentration (15%) showed the highest current densities. According to the higher current densities at high potentials, this cell had the smallest activation overpotential. The ohmic drop was comparable to the cell with 20% PTFE. The bend, starting at current densities of -110 mA/cm² indicates beginning of diffusion limitations. It is assumed that diffusion limitation is strongly related to the solidity and structure of the electrode. This property is affected from procedures (rolling, pressing) during the (manual) electrode preparation wherefore the diffusion limitation varies from electrode to electrode to a certain extent. It was shown that a binder concentration of 25% is too high to allow a proper electrode wetting and the establishment of good three phase boundaries with KOH solutions of 6 molar and less. Therefore, the following measurements were mainly conducted with 15% and 20% of PTFE binder. It appears that the lower binder concentration (15% PTFE) is preferable in a media with exclusively KOH, at least for initial measurements.

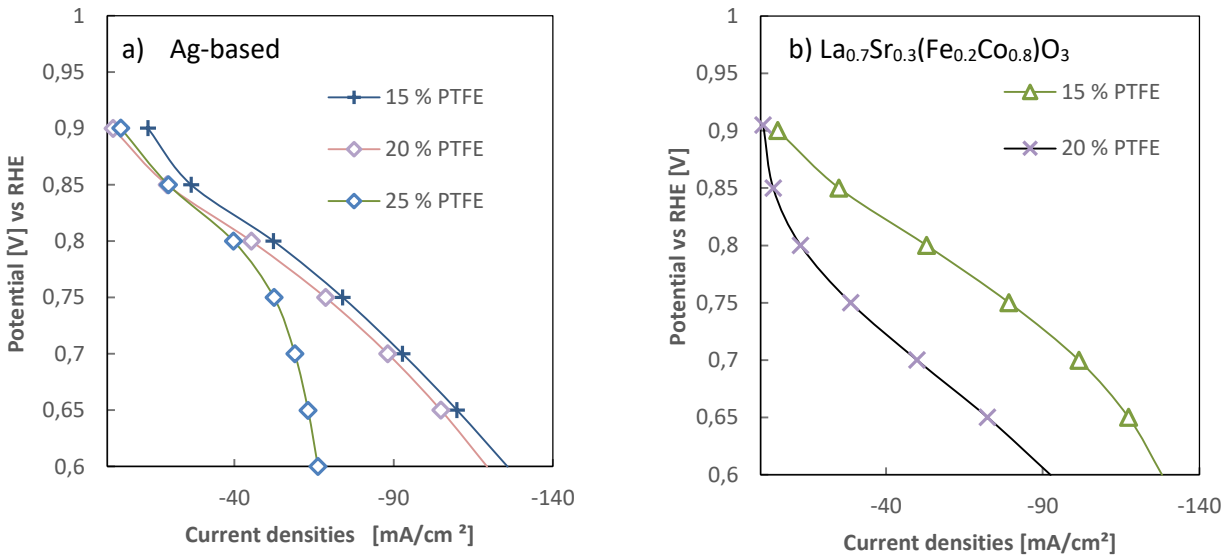

Fig. 17: Initial polarization curves of the a) Ag-based and b) $La_{0.7}Sr_{0.3}(Fe_{0.2}Co_{0.8})O_3$ catalyst with different PTFE amounts.

Fig. 17 shows the initial polarization curves of the $La_{0.7}Sr_{0.3}(Fe_{0.2}Co_{0.8})O_3$ and Ag-based catalyst with varying PTFE contents. It is noted that the Ag-based electrode, with 25 % PTFE, suffered from distinct diffusion limitations, starting at current densities of -40 mA/cm². The polarization curves of the $La_{0.7}Sr_{0.3}(Fe_{0.2}Co_{0.8})O_3$ catalyst represent the electrodes with 15 % and 20 % PTFE binder. Although, three electrodes with 25 % PTFE binder were prepared, it was

not possible to record a polarization curve due to too low currents. It seems, that these electrodes suffered from a lack of the three phase boundaries whereby the electrolyte was not able to wet the GDL sufficiently. Nevertheless, the principle trends are similar to the $La_{0.7}Sr_{0.3}MnO_3$ catalyst. Electrodes with a lower PTFE amount showed a higher initial performance.

4.1.2 Influence of the KOH concentration

To study the influence of the electrolyte concentration on the ORR, half- cell measurements with 1 M, 3 M and 6 M KOH concentrations and various binder concentrations were tested. The resulting polarization curves, of the $La_{0.7}Sr_{0.3}(Fe_{0.2}Co_{0.8})O_3$, the $La_{0.7}Sr_{0.3}MnO_3$ and Ag-based catalyst are shown below.

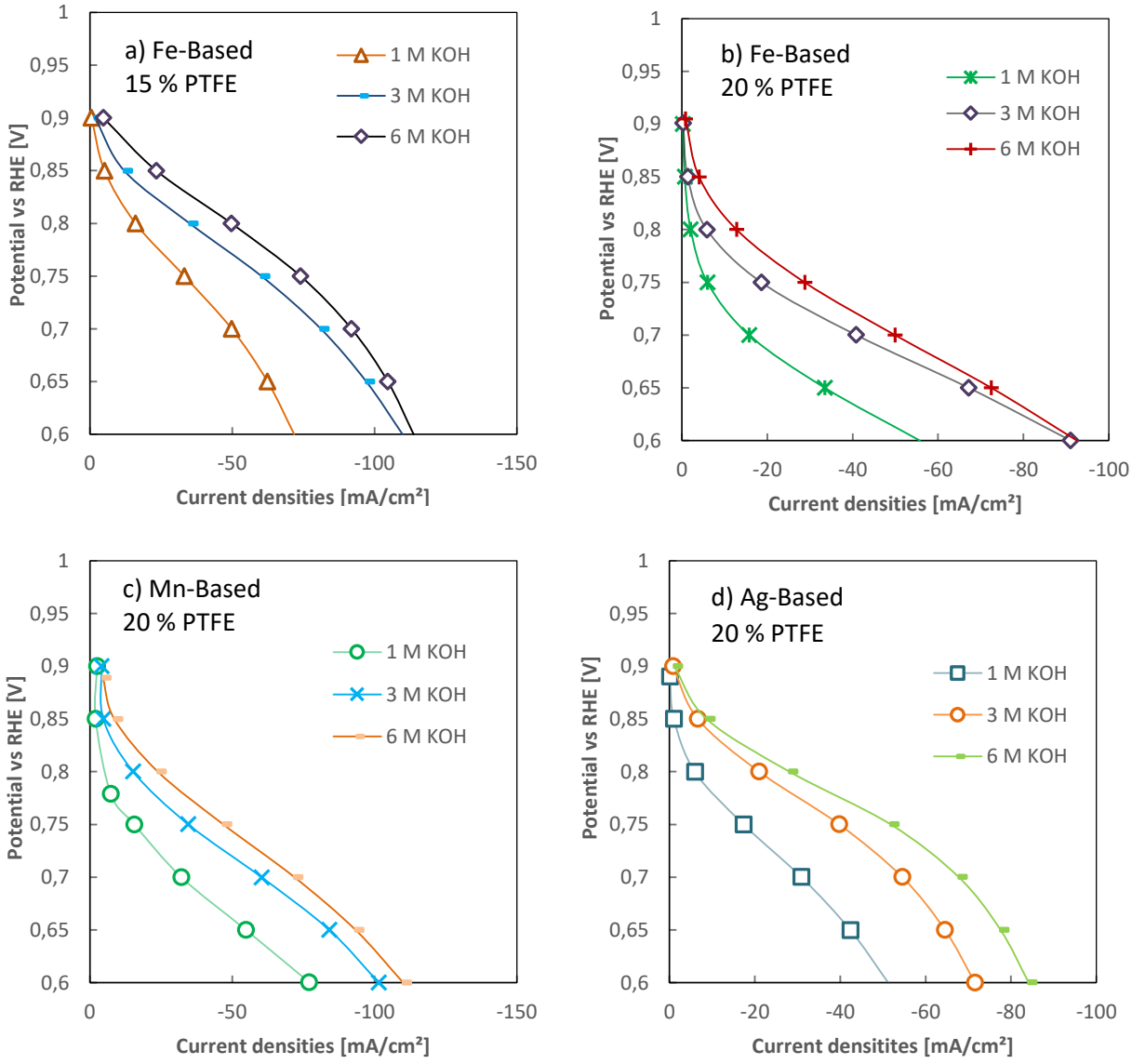

Fig. 18: Polarization curves with various binder contents and electrolyte concentrations

It can be seen, that for the ORR, the current densities have risen with increased electrolyte concentration due to improved mass transport and reduced charge transfer resistance. This is also confirmed by the EIS-resistance measurements (seen in the table below). The electrodes showed only slightly higher performances in 6 M KOH compared to 3 M KOH. This is explained by the conductivity-concentration relationship of KOH electrolytes (as described in section 2.6). At room temperature, the conductivity increases roughly linear at KOH concentrations of 1 M to 3 M. But a further increase in concentration leads to increased resistances due to hindered ion mobility. According to Gilliam et al. and Lolk et al. is the maximum conductivity, at room temperature, reached at a KOH concentration between 6 and 7 M KOH [51,60]. This explains the less distinct performance improvement of the electrodes in 6 M KOH, as seen in Fig. 18. The polarization curves in Fig. 18 a) and b) illustrate that this trend is independent from the binder concentration. Both electrodes showed only a minor performance improvement in 6 M KOH compared to a 3 M KOH electrolyte.

Table 4 gives an overview of the internal resistance and the amount of maximum measured current densities (at 0.6V). It can be seen that the maximum current densities are improving with higher electrolyte concentration and lower binder content.

Table 4: Internal resistances of the cathodes in half-cell set ups and current densities j at 0.6 V vs. RHE at different KOH concentrations and a gas flow of 30 ml/min synthetic air.

	1 M KOH	3 M KOH	6 M KOH
Internal resistance [Ω]	0.21	0.14	0.12
Fe-Cat ,15% PTFE, j at 0.6 V [mA/cm²]	72	110	114
Fe-Cat ,20% PTFE, j at 0.6 V [mA/cm²]	56	93	93
Mn-Cat ,15% PTFE, j at 0.6 V [mA/cm²]	72	83	95
Mn-Cat, 20% PTFE, j at 0.6 V [mA/cm²]	77	101	110
Ag-Cat, 15% PTFE, j at 0.6 V [mA/cm²]	112	127	141
Ag-Cat, 20% PTFE, j at 0.6 V [mA/cm²]	51	71	84

4.1.3 Influence of the oxygen partial pressure

The influence of the O_2 partial pressure was investigated by switching between synthetic air and pure oxygen as cathode feed gas. The measurements were performed with 30 ml/min synthetic air (which contains 20% oxygen) and then with pure oxygen, by using only one fifth of the synthetic air amount (6 ml/min). Thus, it is assured, that the same overall amount of oxygen is fed to the electrode. In case of synthetic air measurements, the partial pressure of oxygen is lower, what led to reduced onset potentials and increased charge transfer, ohmic-drop and overall in a lower cell performance. This can be seen in Fig. 19. The measurements with synthetic air showed 3-4 times lower current densities compared to measurements with pure oxygen. This is attributed to nitrogen as competitive gas.

Some electrodes showed diffusion limitations during the oxygen measurements, even at higher

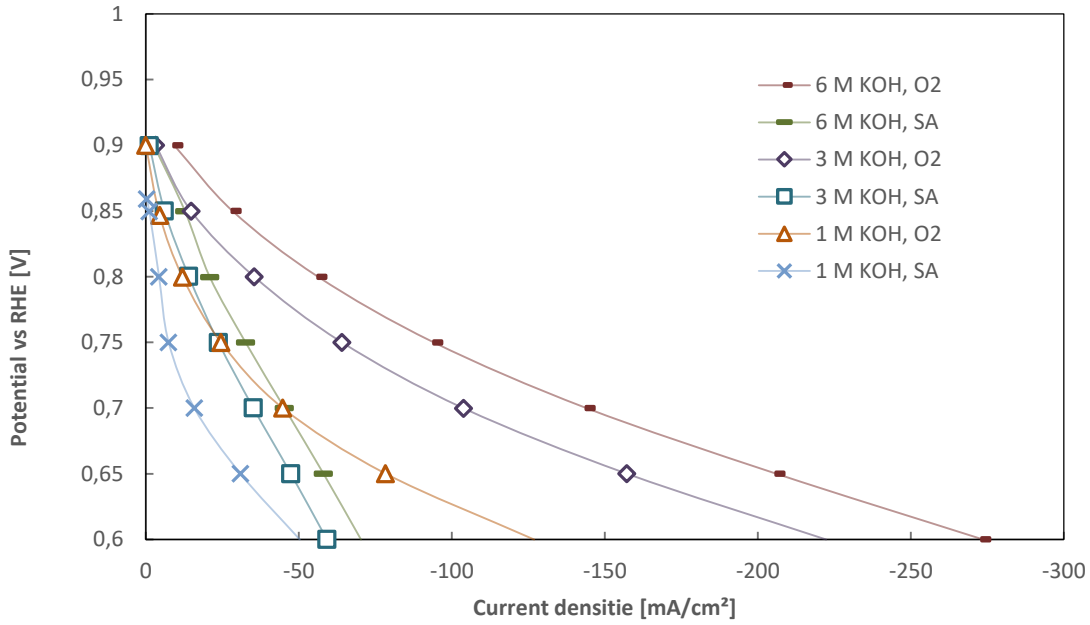

Fig. 19: Polarization curves of the the $La_{0.7}Sr_{0.3}MnO_3$ catalyst with 15 % PTFE, different electrolyte concentrations and O_2 or synthetic air as feed gas.

oxygen flow rates of 12 ml/min. As seen in Fig. 20, the polarization curve with 3 M KOH electrolyte was less diffusion limited at higher current densities compared to the measurement with 6 M KOH. This is likely based on the higher oxygen solubility and diffusion rate in 3 M KOH media [48]. However, this diffusion limitation was not observed in every electrode. The electrode permeability is also depending on process steps during manufacturing. Especially the

rolling process induces a certain variation between the solidity and catalyst loading of electrodes. As a consequence, electrodes, also in the same composition, may show varying diffusion behaviour and cell performances.

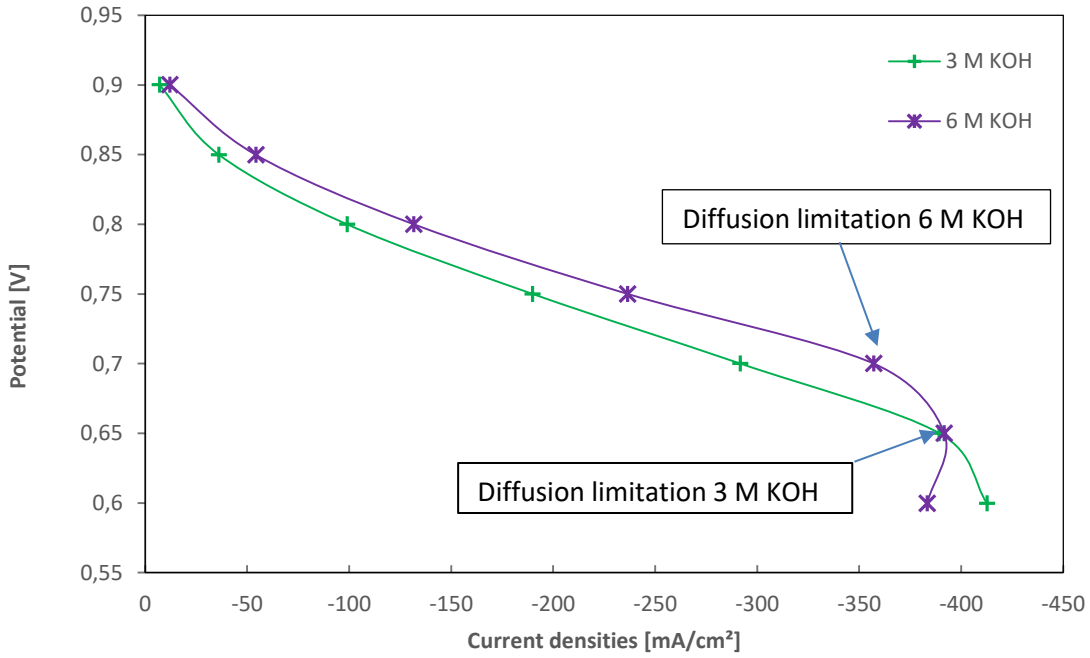

Fig. 20: Diffusion limitations of the $La_{0.7}Sr_{0.3}(Fe_{0.2}Co_{0.8})O_3$ half-cell in 3 M KOH and 6 M KOH and 12 ml/min O_2 feed gas

4.1.4 Influence of the gas flow rate and temperature

The influence of the gas flow rate was investigated by measurements with doubled synthetic air feed gas flow rates. To avoid diffusion limitations, the lower flow rate was set to 50 ml/min, what is high enough to supply the electrodes with excess feed gas. These measurements were conducted at 25 °C and 45 °C to evaluate the temperature influence. The resulting polarization curves of the $La_{0.7}Sr_{0.3}(Fe_{0.2}Co_{0.8})O_3$ and $La_{0.7}Sr_{0.3}MnO_3$ catalyst can be seen in Fig. 21.

The doubling of the flow rate of the Fe-based electrode showed an increase in current density of only 12% at 0.6 V vs. RHE at room temperature. The Mn-based electrode represented a similar performance increase of 14 %. The performance increase, due to doubled flow rate, is in the same range for measurements at 45 °C. It appears, that the flow rate has only minor influence on the cell performance, as long as no diffusion limitations are occurring.

The operating cell temperature, however, has a significant influence on the reaction kinetics and electrolyte conductivity [53]. Thus, the temperature increase of 20 °C showed a current density increase (at 0.6V vs RHE) of around 30 % for both flow rates and the Fe-based electrode. The measured temperature influence was lower for the Mn-based catalyst. The current densities (at 0.6 V vs RHE) increased by 21 % at 50 ml/min and 15 % at 100 ml/min. Table 5 summarizes these findings.

Table 5: Performance increase of the perovskites due to elevated temperature and potential at 0.6 V vs RHE

Catalyst:		Fe-Based	Mn-Based
Increase in current densities at 0.6 V, due to doubled flow rate	@ 25 °C	12 %	14 %
	@ 45 °C	13 %	7 %
Increase in current densities at 0.6 V, due to 20 ° temp. increase	@ 50 ml/min	30 %	21 %
	@ 100 ml/min	31 %	15 %

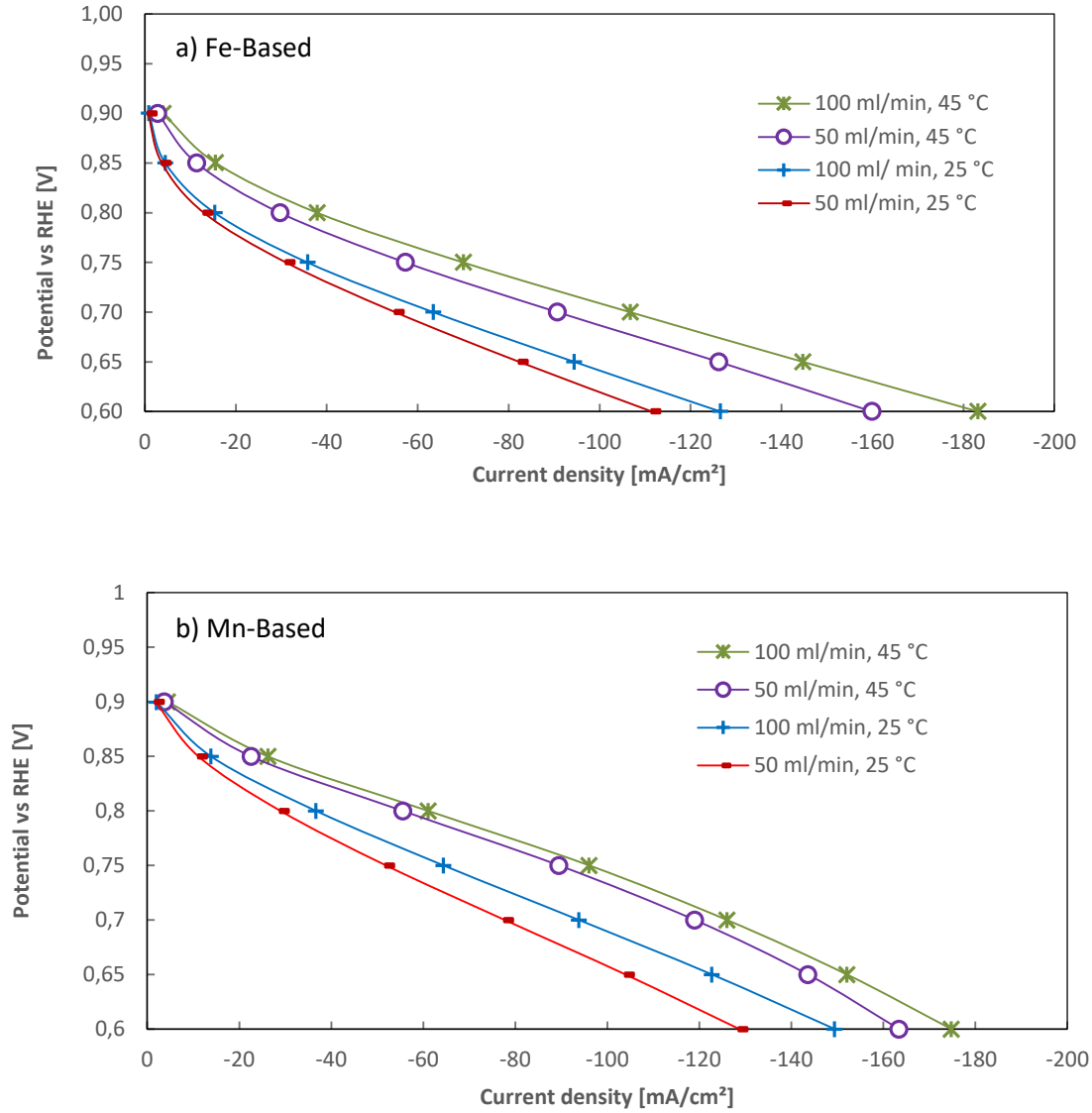

Fig. 21: Polarization curves of a) the $La_{0.7}Sr_{0.3}(Fe_{0.2}Co_{0.8})O_3$ electrode (15 % PTFE) and b) the Mn-based electrode (15 % PTFE) with synthetic air flow rates of 50 and 100 ml/min at 25 °C and 45 °C.

4.2 Stability investigation

The stability investigation was performed for several hundred hours in KOH and a KOH/EtOH mixture. First results showed a certain performance change within the first hours of operation, due to changing three-phase boundaries during the electrode wetting. This is discussed in detail in the following section as conditioning period. The second part of the stability investigation refers to the long-term stability in KOH and the KOH/EtOH mixture.

4.2.1 Conditioning period

At first operation, almost every electrode required a couple of hours to reach a more stable performance. This time period was different for most of the electrodes and lasted up to 9 hours. During this time, it was not possible to operate some cells at high potentials (0.90 V and 0.85 V) due to alternating currents during the measurement. After an operation at lower potentials (0.75 V), the current densities increased first and stabilized after a certain period of time. After this “conditioning period”, a full polarization curve was recordable for these cells. This performance increase within the first few hours is illustrated in Fig. 22. It shows polarization curves of a Mn-based electrode, which allowed full measurements after the initial operation.

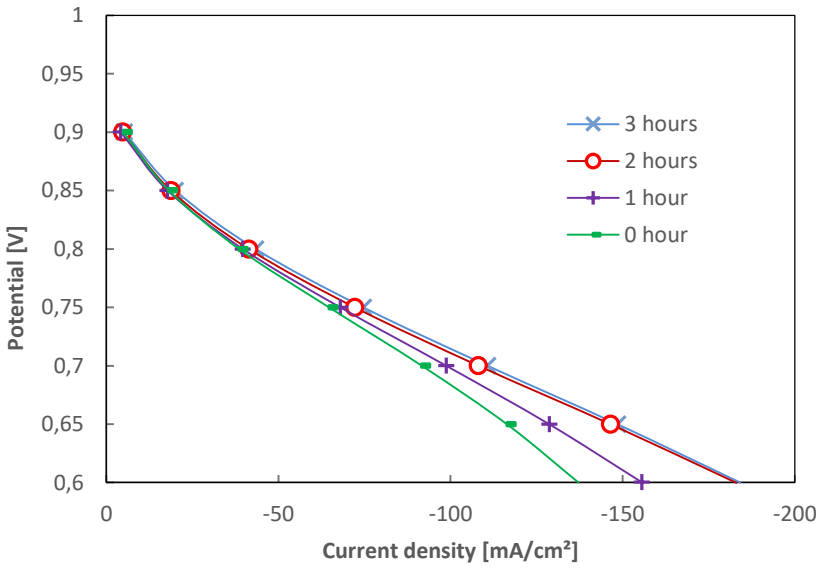

Fig. 22: Performance changes of a $La_{0.7}Sr_{0.3}MnO_3$ electrode (15 % PTFE) within the first few hours of operation

This performance increase expresses the time dependency of achieving sufficient mass transport within the electrode. Depending on the consistence and tightness of the electrode, different activation periods are required to achieve electrolyte soaking of the electrode and the creation of enough three phase boundaries. After this activation time, a more constant cell performance is reached.

4.2.2 Long-term Investigation

After the conditioning period, the durability test could be performed, by using the constant voltage method. Thereby, cathodes were operated at a constant potential of 0.75 V without ethanol

to investigate an emerging performance change caused by alkaline media (6 M KOH). During that, polarization curves were recoded to evaluate occurring performance changes. After some time, ethanol was added. Immediately after the addition of EtOH, polarization curves were recorded to determine performance changes due to the EtOH addition. Similar to the investigation in KOH, long term operations were performed at a constant potential of 0.75 V. In between, polarization curves were recorded in order to investigate the extent of degradation. Both perovskite catalysts showed similar trends in alkaline media. In the following presented perovskite findings refer to both catalysts.

4.2.2.1 Perovskite stability in alkaline media

The $La_{0.7}Sr_{0.3}MnO_3$ and the $La_{0.7}Sr_{0.3}(Fe_{0.2}Co_{0.8})O_3$ catalysts showed similar trends in alkaline media and synthetic fed gas (30 ml/min). Electrodes with 15% PTFE showed a 10-20 % loss in current density at a potential of 0.6 V vs RHE within the first 100 hours (0.1-0.2 %/h). Accordingly, the performance was predominately stable and only minor losses were recorded, as shown in Fig. 23.

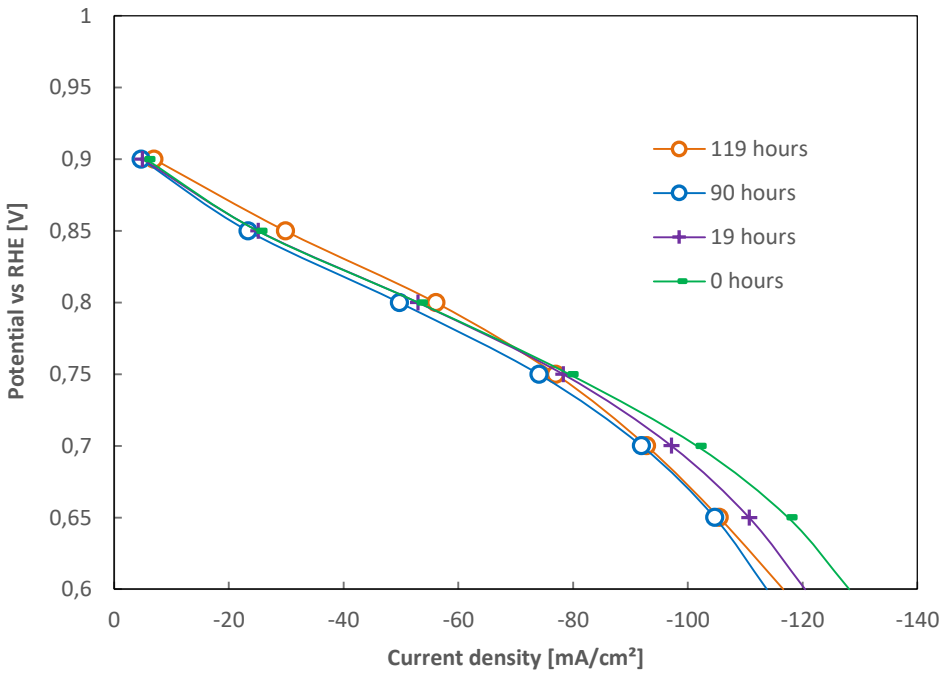

Fig. 23: Polarization curves of the $La_{0.7}Sr_{0.3}(Fe_{0.2}Co_{0.8})O_3$ catalyst with 15 % PTFE, recorded in 6 M KOH during the first 119 hours of operation with 30 ml/min synthetic air .

Perovskite electrodes with 20% PTFE binder showed different results in alkaline media. As shown in Fig. 24, most of the cathodes exhibited around 5 % current density increase at 0.6 V within the first hours of testing, before a constant performance was reached.

This trend is contrary to electrodes with 15% PTFE and is explained by diverse electrode soaking behaviour. Electrodes with 15% PTFE showed a limited soaking effect within the first 50-

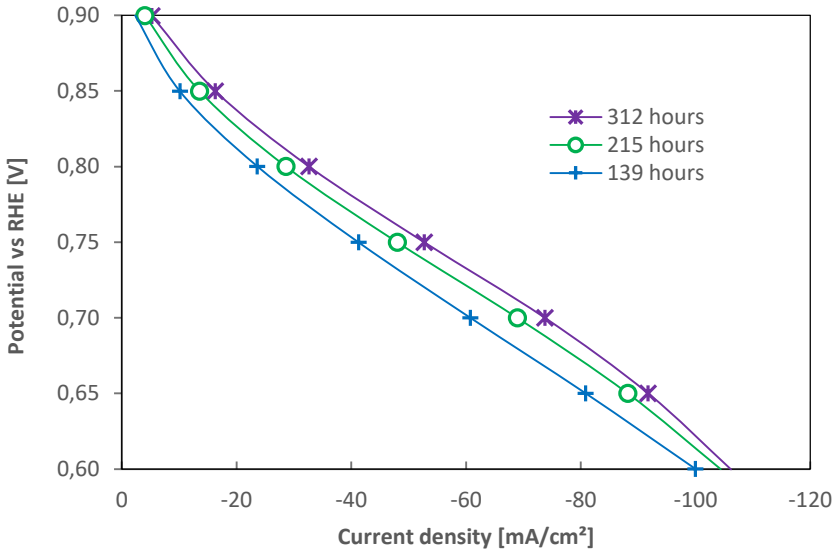

Fig. 24: Polarization curves of the $La_{0.7}Sr_{0.3}MnO_3$ electrode (20 % PTFE), recorded after 139 h, 215 h and 312 h.

100 hours, resulting in a reduced three-phase boundary. However, electrodes with 20% PTFE binder needed a longer wetting period, in order to achieve sufficient soaking of electrolyte. Overall, electrodes with 15% and 20% binder presented a stable operation in alkaline media over hundreds of hours. The comparable low initial performance of the electrodes with 20% binder is partially compensated by temporary performance increase. Electrodes with both binder contents appeared to be stable and no significant influence of the PTFE binder on the long-term stability could be determined.

4.2.2.2 Perovskite stability in alkaline/ethanol media

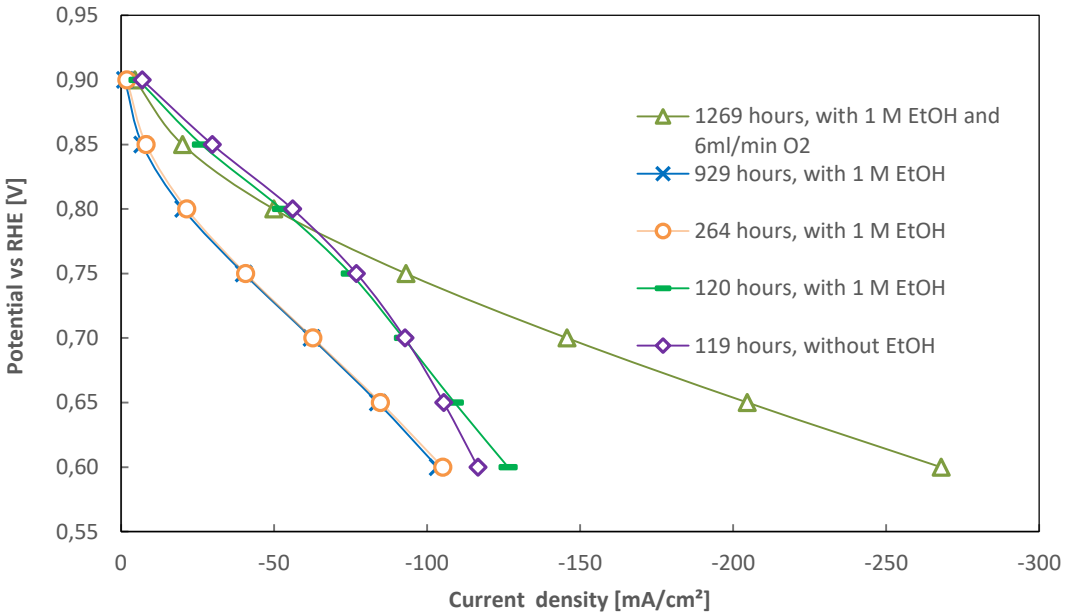

Fig. 25: Polarization curves of the $La_{0.7}Sr_{0.3}(Fe_{0.2}Co_{0.8})O_3$ electrode with 15% PTFE 6 M KOH and 1 M EtOH, after operation times of 110 h (in KOH), 120 h, 929 h and 1269 h (last measurement with 6 ml/min O_2).

After the recording of constant polarization curves, ethanol was added to the electrolyte (1 M EtOH and 6 M KOH mixture). The instantaneously recorded polarization curve, of the 15% PTFE Fe-based electrode, showed a temporary increase of maximum current densities, as seen in Fig. 25.

However, polarization curves during long-term operation revealed a performance loss after the addition of ethanol. The degradation is more distinct at higher potentials, especially in the activation overpotential region. As presented in the figure above, after 145 hours of operation in ethanol the maximum measured current density (at 0.6 V) was reduced by 11 % (0.08 %/h) while the current density at a potential of 0.75 V was lowered by 47 % (0.32 %/h). Afterwards, the cell performance remained stable until the last comparable measurement at 929 hours operation time. After 810 hours in ethanol, the cell shows degradation rates at 0.6 V of 0.01 %/h and 0.06 %/h at 0.75 V. Also, the exchange of the electrolyte-fuel mixture, to overcome ethanol loss due to evaporation, had no significant impact on the stability. The measurement with synthetic air was stopped after 929 hours operation time and was continued with pure oxygen to 1,269 hours overall operation time. The final polarization curve revealed a maximum current density of 268 mA/cm² with oxygen gas feed.

The polarization curves of the Fe-based cathode with 20% PTFE in 1 M EtOH and 6 M KOH are illustrated in Fig. 26. After recording stable performances in alkaline media, ethanol was added. The recorded polarization curves showed, similar to electrodes with 15 % binder, an initial performance increase in maximum current densities, followed by a degradation which stagnated after some time. The performance loss due to the addition of ethanol was around 7 % (0.03 %/h) at 0.6 V, which is comparable to cathodes with 15% PTFE. At potentials above 0.7 V, no losses could be determined.

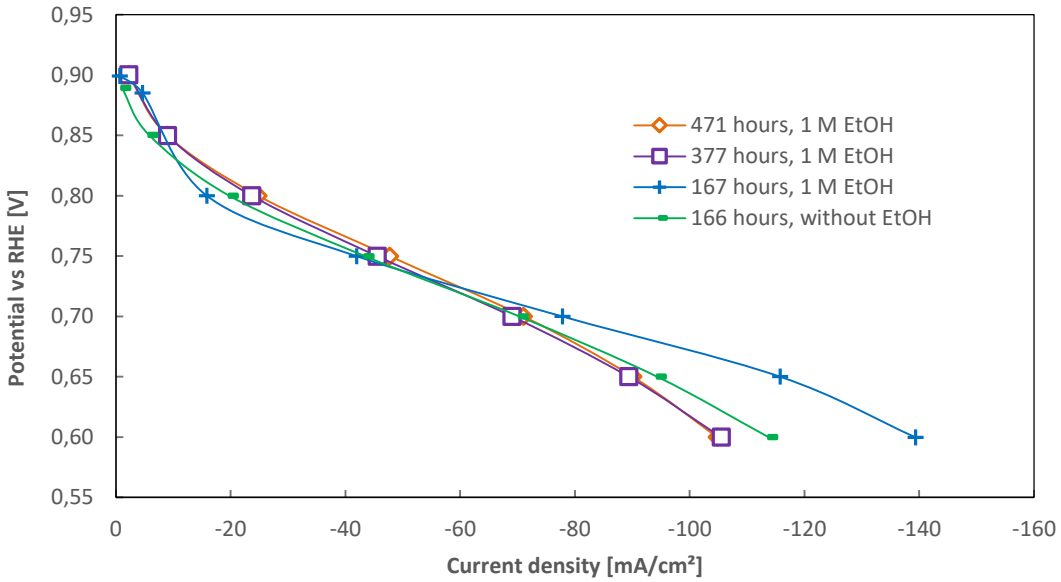

Fig. 26: Polarization curves of the $La_{0.7}Sr_{0.3}(Fe_{0.2}Co_{0.8})O_3$ electrode with 20% PTFE, performed after 166 h (in KOH) and 167 h, 377 h , 471 h (in 6 M KOH and 1 M EtOH).

Fig. 27 shows the stability of the Mn-based perovskite in ethanol. The principle trends are similar to the Fe-based catalyst. However, the polarization curves showed a slightly higher degradation than the Fe-based catalyst. At a potential of 0.6 V, the current densities were reduced by 28 % and at 0.75 V by 45 % after the operation in ethanol. Thus, the degradation rates, during 304 hours in ethanol, were 0.09 %/h at 0.6 V and 0.15 %/hour at 0.75 V.

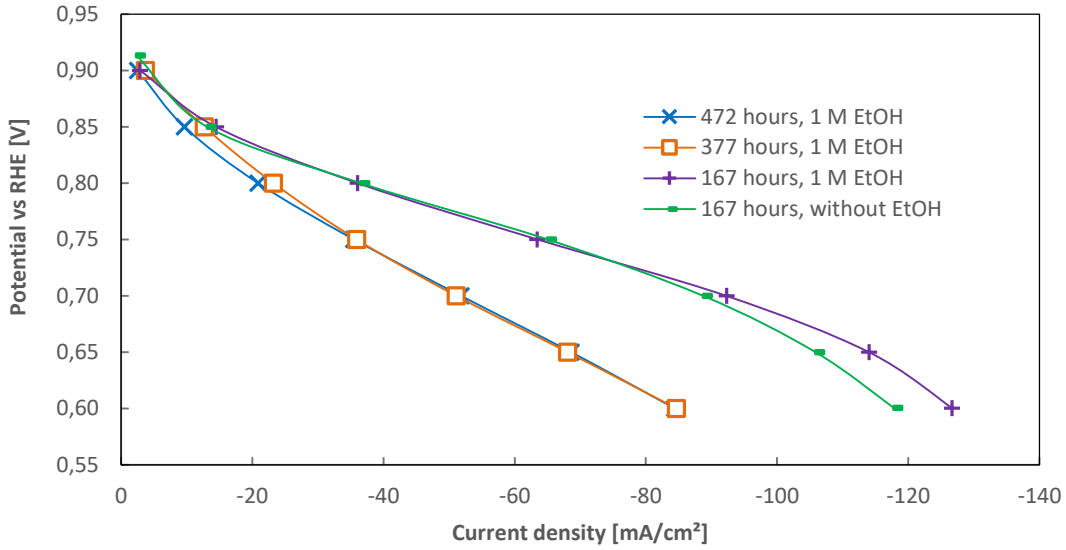

Fig. 27: Polarization curves of the $La_{0.7}Sr_{0.3}MnO_3$ electrode with 20% PTFE, performed after operation times of 167 h (in 6 M KOH) and 167 h, 377 h , 471 h (in 6 M KOH with 1 M EtOH).

4.2.2.3 $AgMn_xO_y$/C catalyst in alkaline media

The $AgMn_xO_y$/C catalyst with 15% PTFE binder showed, compared to the perovskite catalysts, a similar degradation, when operated at a constant potential of 0.75 V vs. RHE in alkaline media. As shown in Fig. 28, the electrode current densities at 0.6 V vs. RHE decreased about

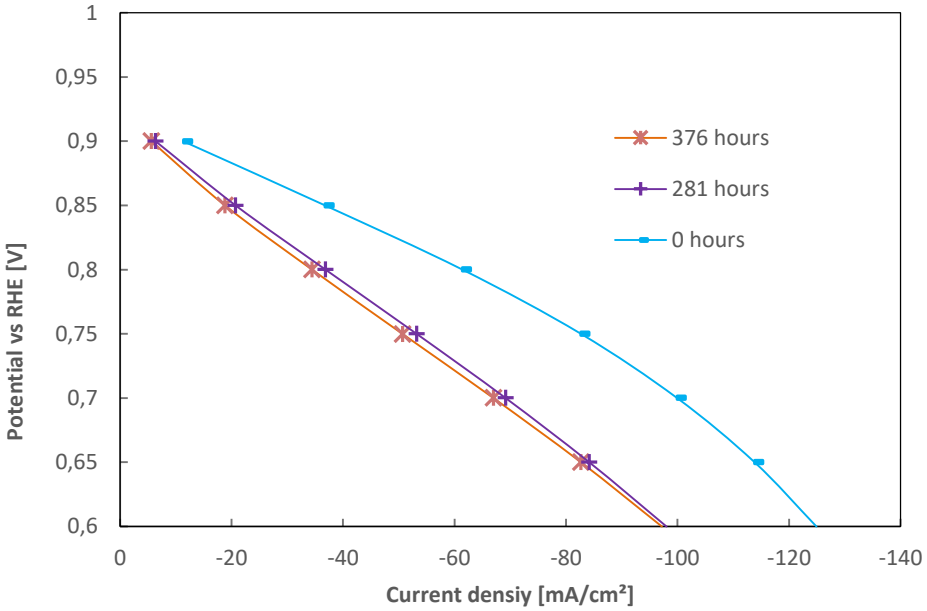

Fig. 28: Polarization curves of the $AgMn_xO_y$/C electrode in alkaline media over 376 hours

20% in the first 280 hours (0.07 %/h) and remained constant until ethanol was added (at 376 hours).

4.2.2.4 $AgMn_xO_y$/C catalyst in alkaline/ethanol media

The polarization curve, recorded after the addition of ethanol (6 M KOH/1 M EtOH mixture), showed a significant instantaneous degradation of 18 % at a potential of 0.6 V vs. RHE. This is illustrated in Fig. 29. As seen by some perovskite measurements, the losses are higher at higher potentials. After 154 hours operation in the ethanol mixture (530 hours of overall operation), another polarization curve was recorded, revealing a performance loss of 52 % compared to operation in KOH only. The polarization curve after another 112 hours (642 hours overall operation time) is almost identical, what demonstrates a stabilization in performance. Therefore, the electrolyte/ethanol mixture was exchanged. The subsequent recorded VI curve showed, again, a high degradation of 60 % compared to the previous measurement. After 48 hours, the last curve was recorded, demonstrating a further continuing degradation.

Overall, the $AgMn_xO_y$/C electrode with 15 % PTFE was operated for 691 hours, therefrom 315 hours in the KOH/ethanol mixture. The measurement showed the establishment of a constant performance in alkaline media for at least 376 hours. However, the addition of ethanol to the electrolyte (to achieve a 1 M solution) resulted in an instantaneous performance loss, which

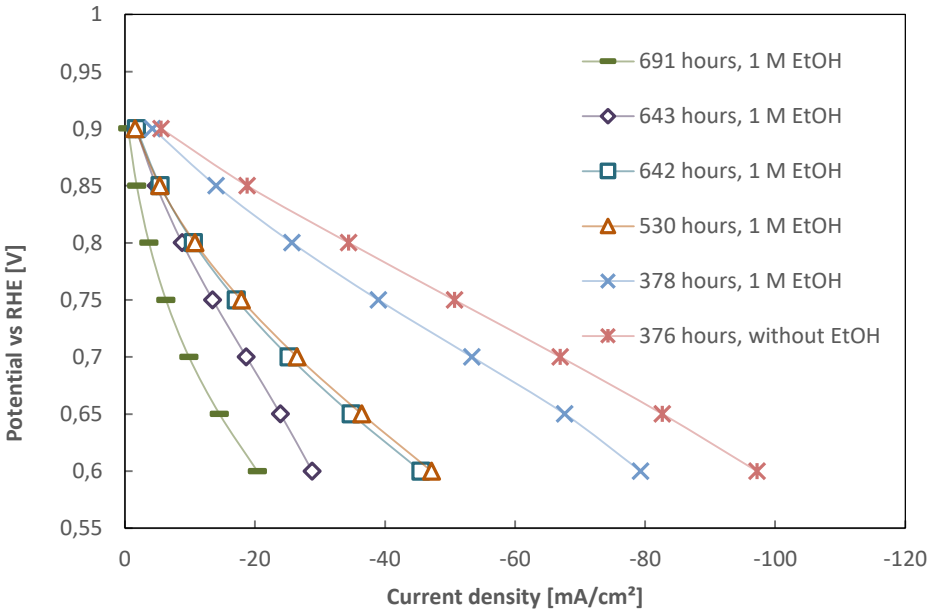

Fig. 29: Polarization curves of the $AgMn_xO_y$/C electrode with 15% PTFE, performed after 376 h (in KOH), 378 h, 530 h, 642 h and 691 h (in KOH and 1 M EtOH).

finally led to an overall performance reduction of 79 % (0.25 %/h) at 0.6 V vs. RHE and 88 % (0.28 %/h) at 0.75 V vs. RHE.

4.3 Catalyst comparison

Fig. 30 shows the polarization curves of the best performing cathodes in alkaline media, at room temperatur and with synthetic air or pure oxygen as feed gas. By the use of synthetic air as feed gas, all catalysts showed a performance in the same range (Fig. 30 a)). However, the $La_{0.7}Sr_{0.3}MnO_3$ perovskite cathode exhibited the highest current density (j) at lower potentials. The better performance was more distinct in the measurement with pure oxygen. A current density of 685 mA/cm² at 0.6 V vs. RHE could be measured. The performance of the $La_{0.7}Sr_{0.3}(Fe_{0.2}Co_{0.8})O_3$ electrode was slightly lower than the Mn-based electrode, besides the region of lower potentials. The appearance of diffusion limitations prevented an adequate comparison. The $AgMn_xO_y$/C catalyzed cathode showed the lowest activation overpotentials and therefore the highest current densities above 0.8 V vs. RHE. However, it appears that, this electrode had also the highest internal resistance, what led to the comparable low current densities below a potential of 0.8 V vs. RHE. Table 6 lists measured current densities at characteristic potentials for comparison.

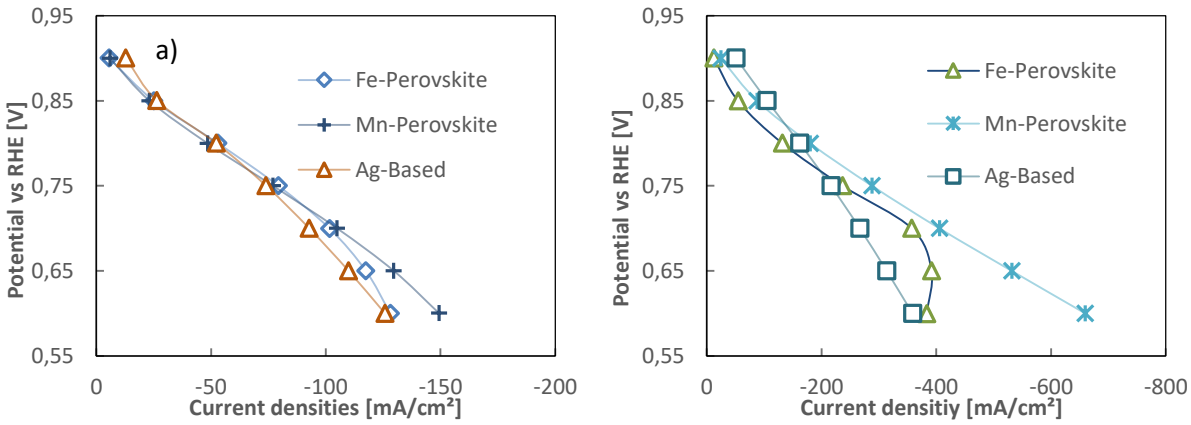

Fig. 30: Best performing polarization curves of the $La_{0.7}Sr_{0.3}(Fe_{0.2}Co_{0.8})O_3$ catalyst (15% PTFE), the $La_{0.7}Sr_{0.3}MnO_3$ catalyst (15% PTFE) and the $AgMn_xO_y$/C catalysts (20% PTFE) with a) synthetic air and b) with pure oxygen

Table 7 compares the catalysts regarding their long-term degradation behavior. All catalysts exhibited a constant performance after 100 – 300 hours of operation with a 6 M KOH electrolyte. The addition of ethanol led to reduced cell performance. Thereby, the electrodes with a

higher binder amount (20 %) showed a higher stability. The Fe-based electrode showed the highest stability with a degradation rate of only 0.03 %/h at 0.6 V. Further details to the findings are discussed in the previous chapter.

Table 6: Comparison of the best performed polarization curves, in regarding their amount of measured current densities (j), with synthetic air and oxygen.

Catalyst	Synthetic air		Pure oxygen	
	j at 0.75 V [mA/cm²]	j at 0.6 V [mA/cm²]	j at 0.75 V [mA/cm²]	j at 0.6 V [mA/cm²]
Fe-Perovskite	79	128	283	383 (Limited)
Mn-Perovskite	77	149	266	659
Ag-Based	74	126	216	358 (Limited)

Table 7: Comparison of catalysts, regarding their long-term degradation behavior in 6 M KOH and a KOH/EtOH mixture.

Catalyst	6 M KOH electrolyte	6 M KOH/1 M EtOH electrolyte	
		Degradation @ 0.75 V vs RHE	Degradation @ 0.6 V vs RHE
Fe-based, 15 % PTFE	Stable after 100 – 300 hours	0.32 %/h	0.08 %/h
Fe-based 20 % PTFE		Not observable	0.03 %/h
Mn-based, 20 % PTFE		0.15 %/h	0.09 %/h
Ag-based, 15 % PTFE		0.25 %/h	0.28 %/h

4.4 Fuel cell measurements

The fuel cell measurements were performed with reproductions of the most promising cathodes of the half-cell measurement series. These were the $La_{0.7}Sr_{0.3}(Fe_{0.2}Co_{0.8})O_3$ and $La_{0.7}Sr_{0.3}MnO_3$ perovskites with 20% PTFE binder. The $AgMn_xO_y/C$ catalyst showed an insufficient stability in the presence of ethanol and was therefore not used. In this experiment, the perovskite cathodes suitability to operate under full-cell conditions, was investigated. Besides, a short-term stability investigation over approximately 24 hour in 1 M and 2 M ethanol was performed and the influence of the operating temperature was analysed. The internal resistance (0.20 Ω) of the fuel cell was used not used to correct the potentials.

The set-up of the experiment was simple and similar to the half-cell measurements, due to the use of a liquid electrolyte and selective cathode catalysts. Only a polypropylene separator was additionally used to avoid possible short-circuits and oxygen cross-over to the platinum containing anode[2]. In order to assemble the cell, cathodes with 20% PTFE binder (40 $mg_{perovskite}/cm^2$) were combined with a PtRu anode (2.5 mg_{Pt}/cm^2 platinum). The electrolyte-fuel mixture was pumped through the cell with a flow rate of 3 ml/min. As feed gas, pure oxygen was used. A lugging capillary was used to track the anode potential, wherefrom the cathode potential was calculated. Before the actual fuel cell measurement took place, the cathodes were operated in 6 M KOH for at least 16 hours to avoid initial performance variations in the conditioning phase (as described in 4.2.1). After that, both catalysts exhibited similar polarization curves, as seen in Fig. 31.

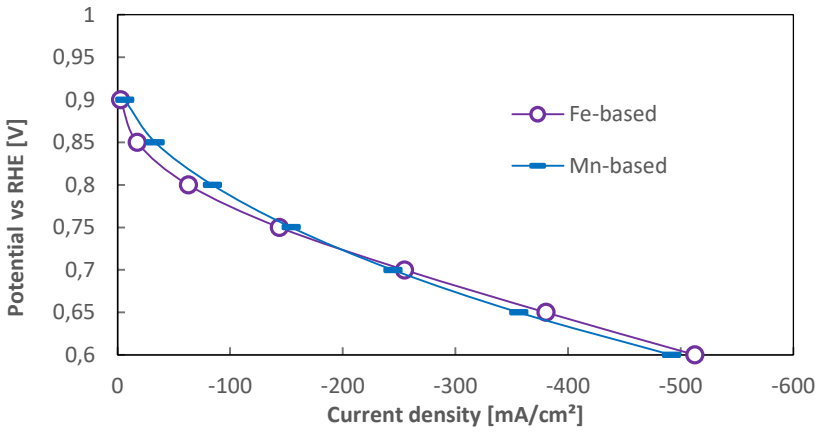

Fig. 31: Half-cell polarization curves of the perovskites which were used in the full cell measurement (with O_2 as feed gas)

[2] Platinum is also a good ORR catalyst and the formation of mixed potentials would lower the cell performance [39].

The fuel-cells were operated first in 6 M KOH and 1 M Ethanol at room temperature. Fig. 32 shows the initial performance of the cell with the $La_{0.7}Sr_{0.3}(Fe_{0.2}Co_{0.8})O_3$ electrode. The open circuit voltage appears to be extraordinarily high (0.98 V). This was also noticed by Grimmer et. al in a similar measurement [61]. Therefore, the calculated cathode potential had a high value from > 1.0 V (with anode OCP of 0.21 V). The maximum power density (mPD) was 15.3 mW/cm² at a current density of 51.0 mA/cm². At this point, the cell voltage was 0.30 V due to the high anode potential of 0.61 V. The corrected cathode potential at the maximum power (mp) was 0.98 V.

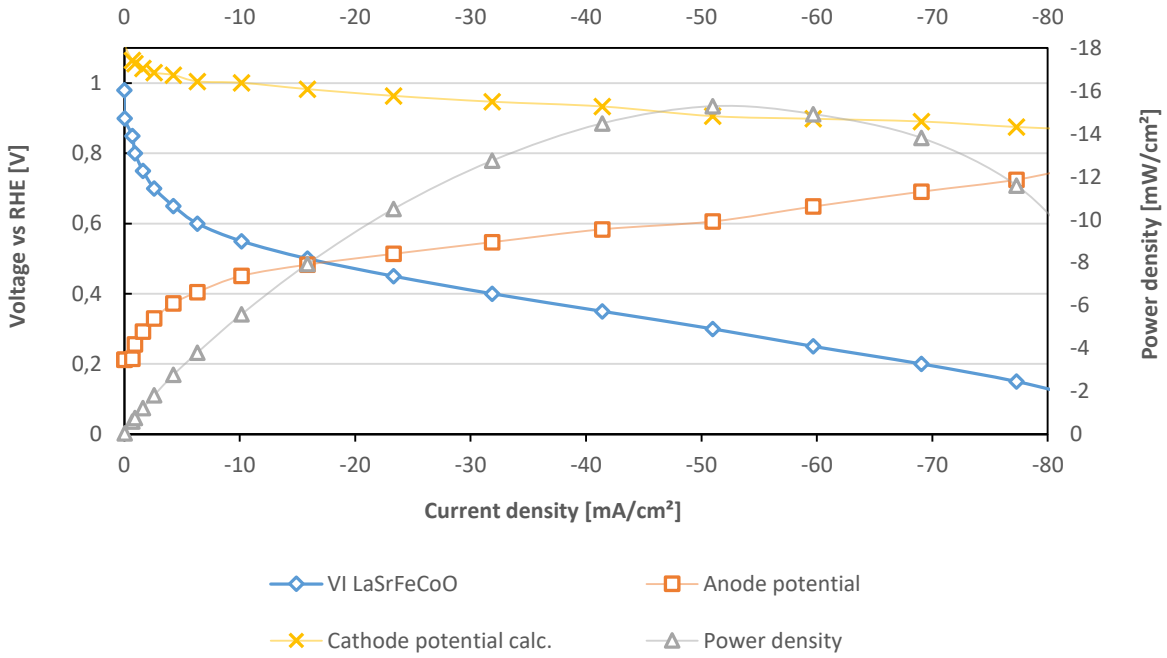

Fig. 32: Results of the initial fuel-cell measurement with the $La_{0.7}Sr_{0.3}(Fe_{0.2}Co_{0.8})O_3$ electrode using a 6 M KOH and 1 M EtOH electrolyte.

Fig. 33 shows the first polarization curve of the cell with the $La_{0.7}Sr_{0.3}MnO_3$ catalyst. Overall, the cell showed a similar performance. The open cell voltage (1.00 V) and peak power density (17.2 mW/cm²) were slightly higher compared to the cell with the $La_{0.7}Sr_{0.3}(Fe_{0.2}Co_{0.8})O_3$ catalyst. However, this is mainly caused by a better anode performance. This is also seen by the lower anode OCP of 0.15 V.

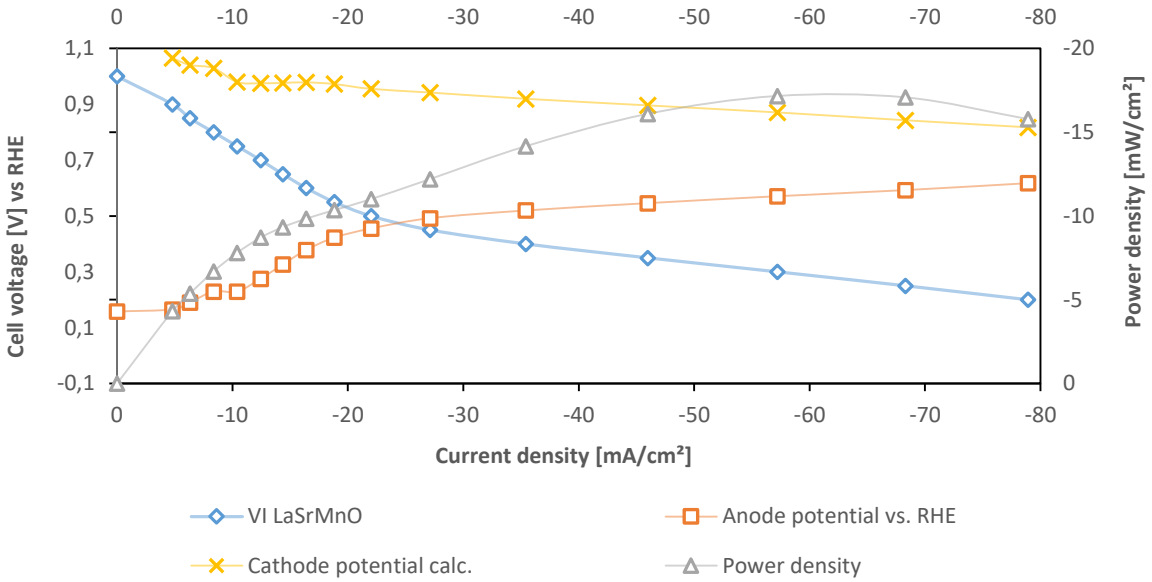

Fig. 33: Results of the initial fuel-cell measurement with the $La_{0.7}Sr_{0.3}MnO_3$ electrode using a 6 M KOH and 1 M EtOH electrolyte.

Both catalysts showed similar performance in the full cell measurements. Power densities (PD) around 15-17 mW/cm² seem to be quite good and comparable to literature [35]. It has to be considered that the measurement was performed at room temperature and with a 1 molar fuel concentration. Moreover, the anodes were prepared without any special treatment and similar to the cathodes. The cathodes were not really stressed in performance aspects, as seen by the calculated half-cell potential. The main performance limitation of the fuel cell was the anode. The table below summarizes the initial performances of the perovskite cathodes.

Table 8: Results of the initial fuel cell measurement with the perovskite cathodes at the maximum power point (mp).

Cathode catalyst	OCV [V]	Cell voltage mp [V]	Cathode (calc.) at mp [V]	mPD [mW/cm²]	CD at mp [mA/cm²]
$La_{0.7}Sr_{0.3}(Fe_{0.2}Co_{0.8})O_3$	0.98	0.3	0.93	15.3	51.0
$La_{0.7}Sr_{0.3}MnO_3$	1.00	0.3	0.89	17.2	57.2

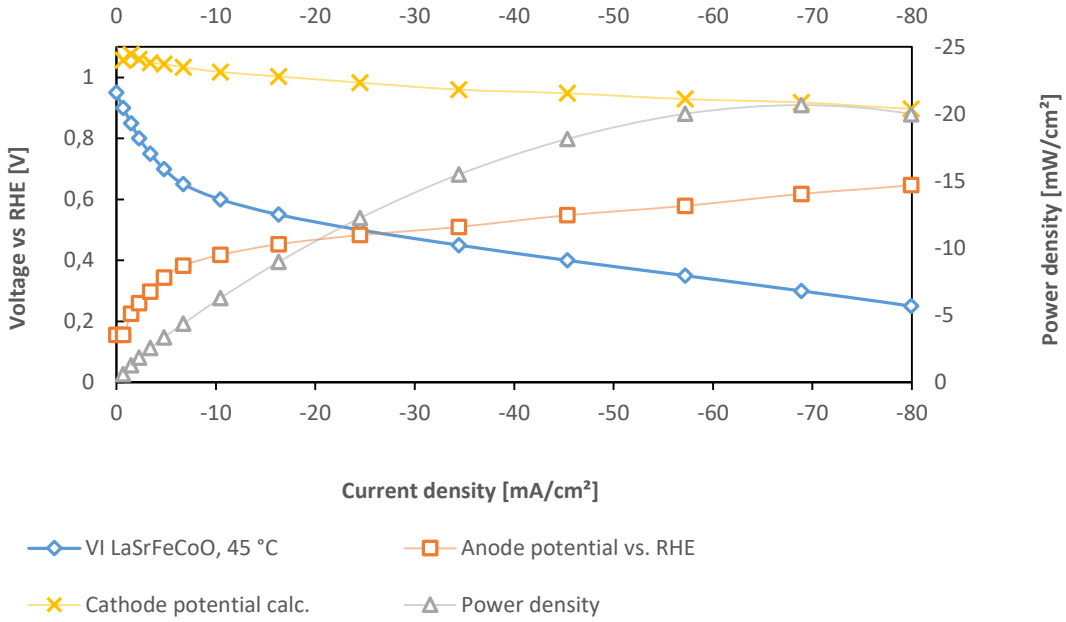

Fig. 34: Polarization and power curve of the Fe-based fuel cell at 45 °C, recorded anode and calculated cathode potential

Subsequently after the measurement at room temperature, the fuel cell with the $La_{0.7}Sr_{0.3}(Fe_{0.2}Co_{0.8})O_3$ catalyst was heated up to 45 °C and another polarization curve was recorded (Fig. 34). This cell achieved a peak power performance of 20.7 mW/cm², what is quite acceptable, considering the use of a 1 molar fuel mixture. This equates an increase of 26 %, which was mainly caused by an improved anode performance.

The Mn-based fuel cell measurement at 45 °C was performed with an electrolyte with a 2 M ethanol concentration. In comparison to a subsequently before recorded measurement at room temperature with a 2 M ethanol solution, the performance increased by 38 % due to elevated temperature.

Besides, a short term stability investigation was performed for 6-8 hours in 6 M KOH and 1 M ethanol and more than 14 hours in 6 M KOH and 2 M ethanol. Thereby, the cells were operated at constant voltages at the maximum power (0.3 V vs. RHE). In 1 M ethanol and 45 °C the cell with the $La_{0.7}Sr_{0.3}(Fe_{0.2}Co_{0.8})O_3$ catalyst revealed a peak performance loss of 3.3 % (0.56 %/h). In contrast to that, the $La_{0.7}Sr_{0.3}MnO_3$ cell was operated for 8 hours at room temperature. It revealed a performance increase of 6.4 % (0.8 %/h). According to the high and constant cathode potential above 0.9 V vs. RHE, these performance changes were mainly caused by the

anodes. The stable operation of the cathodes in a 6 M KOH and 1 M ethanol media is also confirmed by results from the half-cell long-term measurements.

However, the operation in 2 M ethanol caused a distinct degradation. After 14 hours of operation of the $La_{0.7}Sr_{0.3}(Fe_{0.2}Co_{0.8})O_3$ cell showed a degradation of 47 % (3.4 %/h) in peak performance. The cell with the $La_{0.7}Sr_{0.3}MnO_3$ catalyst performed better. It showed a peak performance degradation rate during 20 hours of 1.9 %/h. On the contrary to the measurement in 1 M ethanol, the cathodes were an additional cause of the fuel cell degradation.

This can also be seen at the lowered OCP and curve shape of the cathode potentials in Fig. 35, which shows the cell at the end of the measurement series. The calculated cathode potential showed increased activation overpotentials and increased ohmic resistances. The operation with a pumped 2 M ethanol and 6 M KOH solution seems to remain a challenge for this type of cathode. Table 9 summarizes the results of the stability investigations.

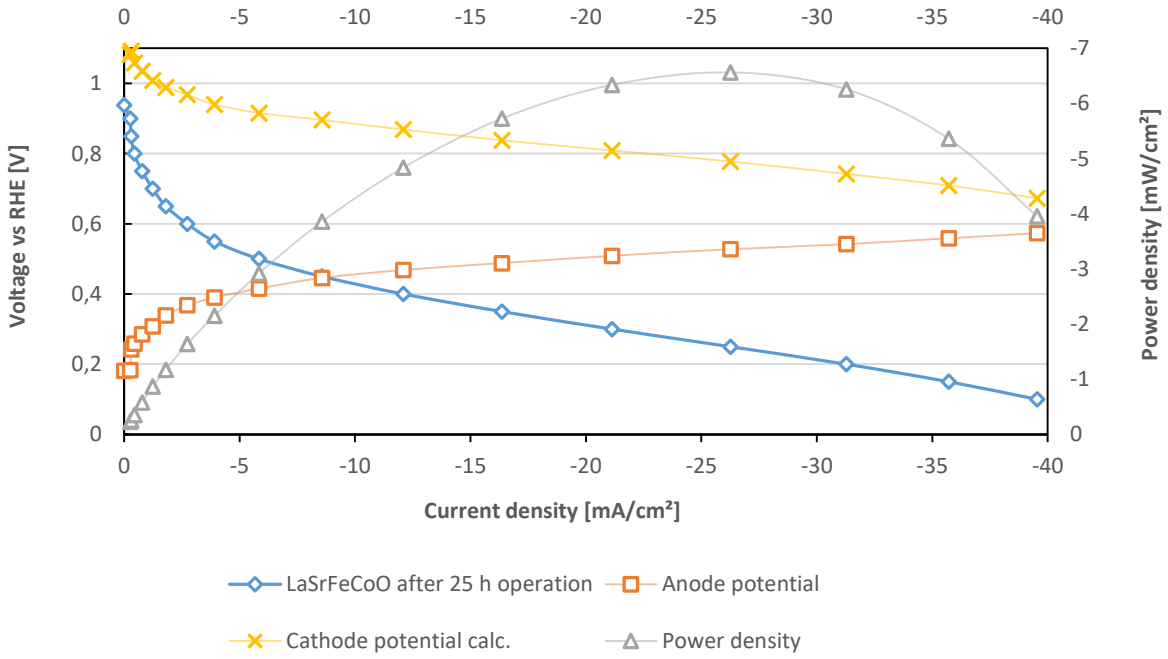

Fig. 35: Fuel cell polarization curve with the $La_{0.7}Sr_{0.3}(Fe_{0.2}Co_{0.8})O_3$ cathode after 25 h operation (14 hours in 2 M EtOH, 11 hours in 1 M EtOH)

Table 9: Degradation rates of the fuel cells in 1 M and 2 M ethanol

Catalyst	Peak Power loss [%/h] in 1 M EtOH	Peak Power loss [%/h] in 2 M EtOH
$La_{0.7}Sr_{0.3}(Fe_{0.2}Co_{0.8})O_3$	- 0.56	- 3.4
$La_{0.7}Sr_{0.3}MnO_3$	+ 0.8	- 1.9

4.5 Ex-Situ characterization (RDE)

The ex-situ characterization was performed with a rotating disk electrode (RDE). This cyclic voltammetry technique is the method of choice to achieve comparable results for the ORR kinetics. It is a reproducible and fast method which requires only small amounts of catalyst [46]. The resulting cyclovoltammograms (CV) of the experiment, which are presented below, show the cathodic sweep as a function of applied potential at different rotation rates. All given potentials refer to the RHE potential which corresponds to the applied potential. Due to the low internal resistance (5 Ω), no potential correction was performed. As usual, the measured currents increased with rising rotation rates due to thinner diffusion layers. These currents were normalized to the geometric area of the electrode (0.196 cm^2). The illustrated ORR curves were corrected by a base CV, measured in N_2 saturated electrolyte.

The polarization curves of the perovskite catalysts can be found in Fig. 36. Both perovskites appear as a combination of two sigmoidal curves. Tulloch and Donne propose that single step reduction process should be observed as a straight forward sigmoidal curve. Therefore, the combined sigmoidal shape indicates the parallel appearance of a two- and four- electron transfer in the ORR. The catalyst disproportion reaction of the peroxides extents the two electron pathway to achieve a 2+2 electron pathway [41]. The collected limiting current densities were higher for the $La_{0.7}Sr_{0.3}MnO_3$ (1.93 mA/cm^2_{geo}) catalyst compared to the $La_{0.7}Sr_{0.3}(Fe_{0.2}Co_{0.8})O_3$ (0.809 V, 1.21 mA/cm^2_{geo}) catalyst, although the base CV is more distinct. The onset potentials of both catalysts were around 0.81 V.

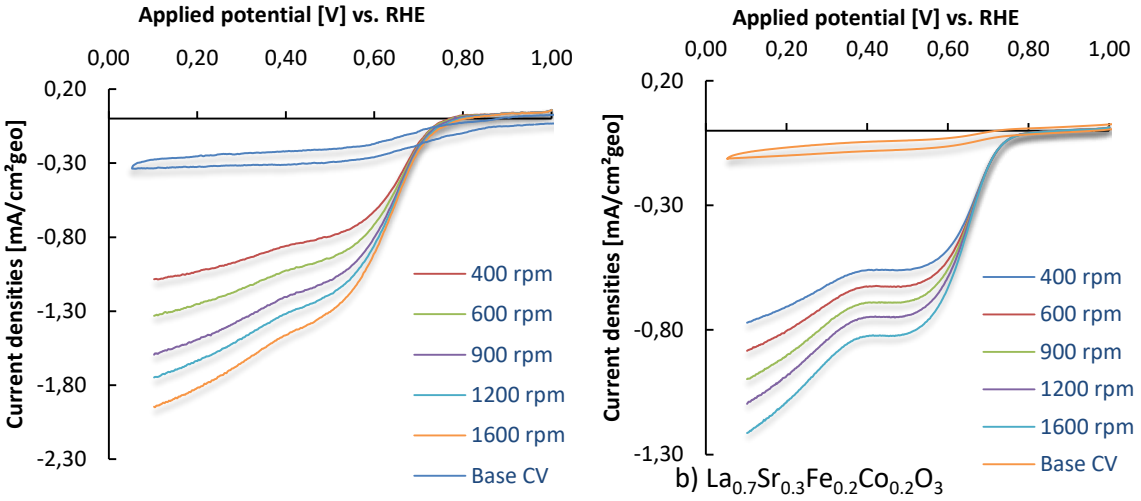

Fig. 36: RDE measurements of a) the $La_{0.7}Sr_{0.3}MnO_3$ perovskite and b) the $La_{0.7}Sr_{0.3}(Fe_{0.2}Co_{0.8})O_3$ perovskite

In contrast to the perovskite catalysts, the cyclovoltammograms of the $AgMn_xO_y/C$ catalyst appears as a typical straightforward sigmoidal curve as seen in Fig. 37. Tang et al. suggest by their ORR measurement of this catalyst, the occurrence of a direct 4-electron pathway [58]. The high onset potential (0.91 V) and limiting current density of 2.22 mA/cm^2_{geo} demonstrate the good ORR activity of this catalyst in alkaline media.

The correlation between the rotation rate and the thickness of diffusion layers were used to perform a Koutecky-Levich analysis to determine characteristic reaction parameters.

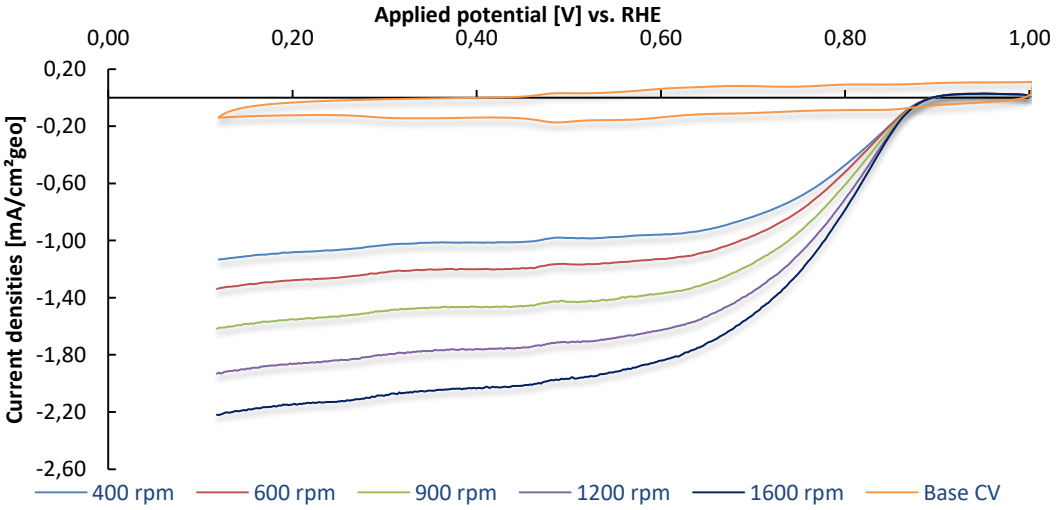

Fig. 37: RDE measurements of the $AgMn_xO_y/C$ catalyst

Fig. 38 below compares the ORR activity of the three catalysts, including the Koutecky-Levich plot. The number of transferred electrons (n) was deviated from the slope and the heterogeneous rate constant (k_h) from the intercept of the Koutecky-Levich plot, performed in the diffusion controlled region (at a potential of 0.1 V). Therefrom it was possible to determine the number of transferred electrons which was determined above 2 for all catalysts (around 2.5).

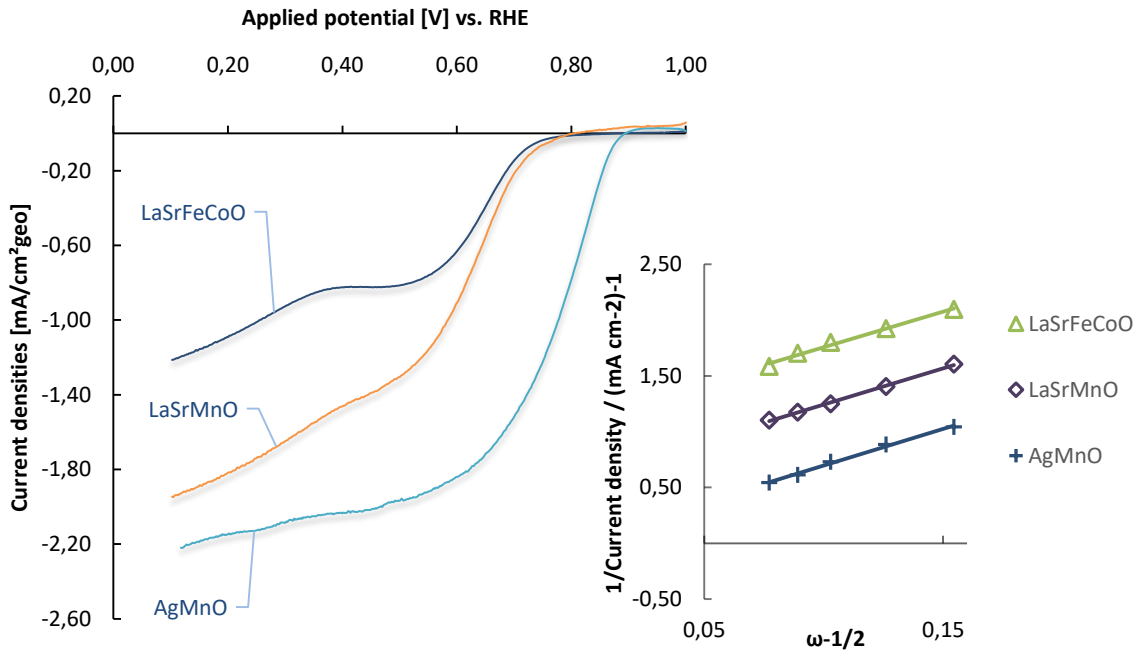

Fig. 38: Comparison of the RDE measurements, the insert represents the Koutecky-Levich plot of all three catalysts.

The number of transferred electrons is proposed elsewhere by little less than 4-electrons for the AgMnO and $La_{0.7}Sr_{0.3}MnO_3$ catalyst [41,45,58]. The parallel line of the $La_{0.7}Sr_{0.3}(Fe_{0.2}Co_{0.8})O_3$ catalyst in the Koutecky plot indicates the occurrence of 4-electron kinetics regarding molecular oxygen [62]. Table 10 summarizes the achieved data from the Ex-situ characterization.

Table 10: Results from the ex-situ characterization of the Fe-based, the Mn-based and Ag-based catalyst.

Catalyst	Transf. n	Rate constant k_h	Onset potential [V]	Limit. current densities [mA/cm²$_{geo}$]
$La_{0.7}Sr_{0.3}MnO_3$	2.74	0.05	0.81	1.92
$La_{0.7}Sr_{0.3}(Fe_{0.2}Co_{0.8})O_3$	2.4	0.01	0.79	1.21
$AgMn_xO_y$	2.56	0.22	0.90	2.22

For an appropriate comparison, it has to be mentioned that the $AgMn_xO_y$ catalyst contains, due to its preparation method, carbon. The RDE measurements of the perovskites were performed without the addition of carbon, to investigate the pure substance. Poux et al. stated, that the addition of carbon to perovskites (such as $La_{0.8}Sr_{0.2}MnO_3$) were leading to a strong drop in the amount of detected peroxides and an improved electrical contact within the catalyst layer. As a result the ORR performance is increased [57]. Nevertheless in this ex-situ method, the $AgMn_xO_y$ catalyst, outperforms the perovskite catalysts regarding the measured current densities, the heterogeneous rate constant and the onset potential.

4.6 Physical characterization

4.6.1 SEM result of Electrode investigations

Scanning electrode microscopy was used to investigate the surface of the perovskite electrodes and the catalyst powder. Electrode samples were taken and analysed before sintering, after sintering (which is also before operation) and after the stability measurement in fuel-cell operation. This should give insides of the sintering influence and the effect of degradation on the electrode surface.

The SEM images below show the morphology of the $La_{0.7}Sr_{0.3}(Fe_{0.2}Co_{0.8})O_3$ electrode. Fig. 39 c) and b) present the electrode before and after sintering. It can be seen that the sintering process enhances the PTFE cross-linking. Both states show the presents of many fine particles (< 1 µm) and so called mud- cracks around 2 µm. The electrode, shown in a), was used

in the fuel-cell experiment. It suffered from significant degradation during the stability measurement. The majority of the fine particles, as seen in b) and c), are lost and mud-cracks are more distinct (20-5 µm). Nevertheless, the PTFE network is still visible, holding the electrode together.

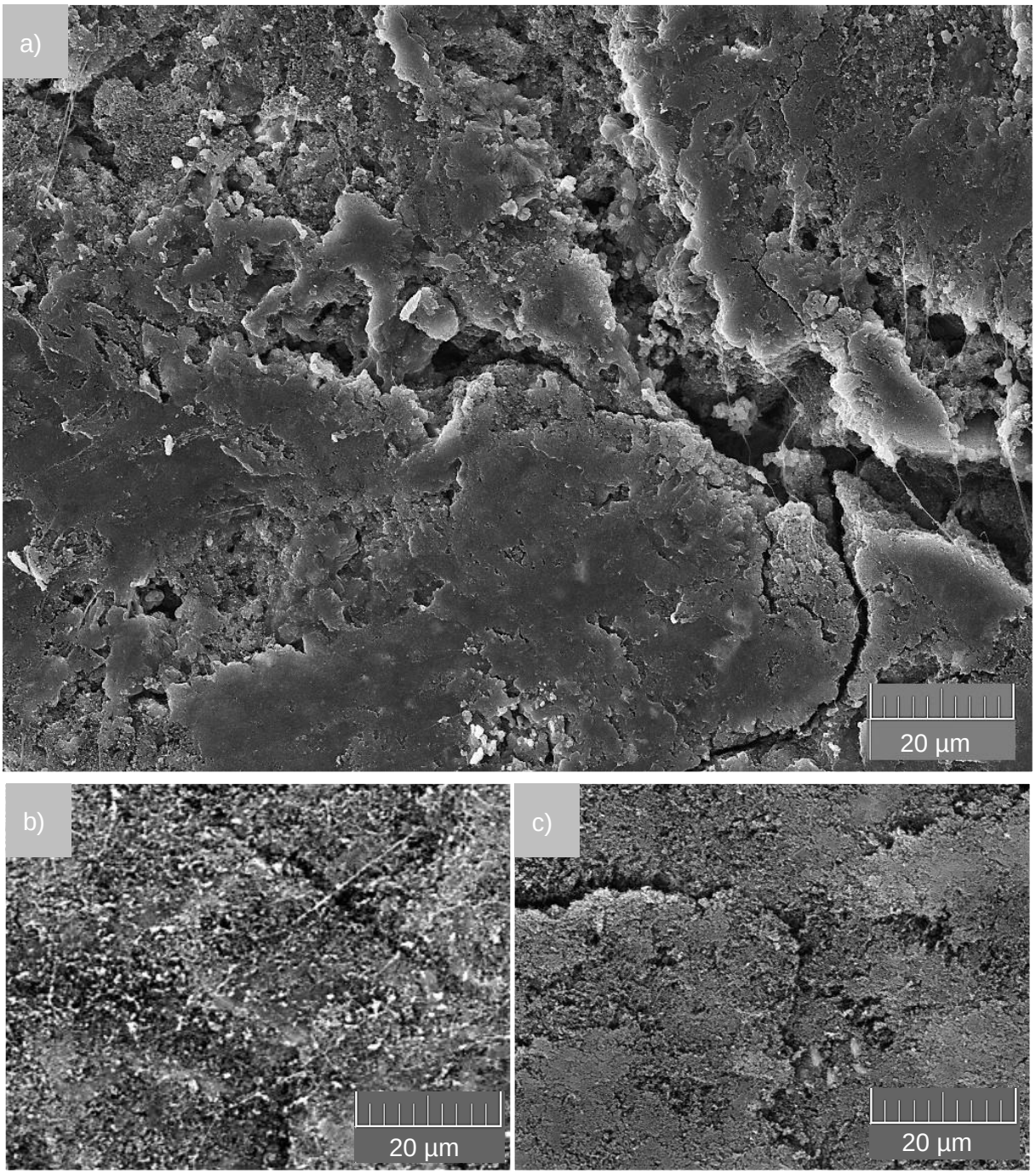

Fig. 39: SEM images of the $La_{0.7}Sr_{0.3}(Fe_{0.2}Co_{0.8})O_3$ electrode, a) after the stability measurement, b) before the operation (after the sintering), c) before the sintering

Fig. 40 shows sections of the surface from the $La_{0.7}Sr_{0.3}MnO_3$ electrode. The particles size distribution seems to be higher for this electrode if compared to the $La_{0.7}Sr_{0.3}(Fe_{0.2}Co_{0.8})O_3$

electrode. Agglomerates from up to 30 µm can be seen, what indicates insufficient grinding. Fig. 40 a) shows the electrode after the stability measurement in the full-cell experiment. As seen in this image, the electrode was not fully freed from KOH electrolyte before it was dried. This led to the formation of KOH crystals which penetrated the electrode structure. This may also occur when the cell is dried out due to electrolyte leakage, or the electrolyte is solidified (due to solvent evaporation or undercooling). The surface itself shows less cracks than the surface of the $La_{0.7}Sr_{0.3}(Fe_{0.2}Co_{0.8})O_3$ electrode. Also, the PTFE linkage is barely visible. As seen before, the sintered electrode reveals a more distinct PTFE network than the non-sintered.

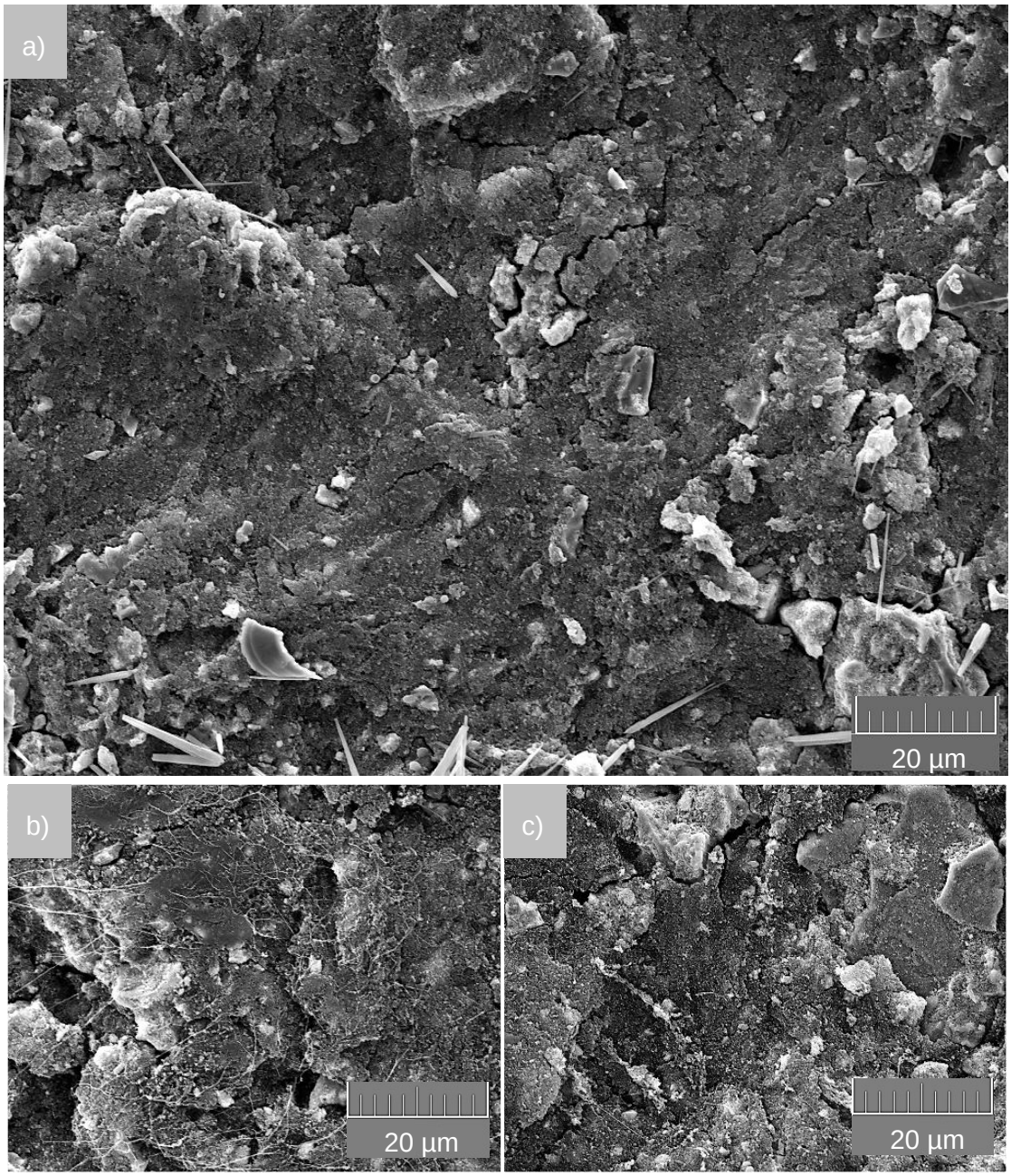

Fig. 40: SEM images of the $La_{0.7}Sr_{0.3}MnO_3$ electrode, a) After the stability measurement, b) before the operation (after the sintering), c) before the sintering

4.6.1.1 SEM results from the bulk catalysts

The SEM analysis from the perovskite catalyst powders are published by Grimmer et al. and are shown in Fig. 41 [61]. Thereby, the Mn-based perovskite structure appears fringed with finer particle size, what provides a greater surface area compared to the $La_{0.7}Sr_{0.3}(Fe_{0.2}Co_{0.8})O_3$ catalyst, which has a more defined, grain-like structure.

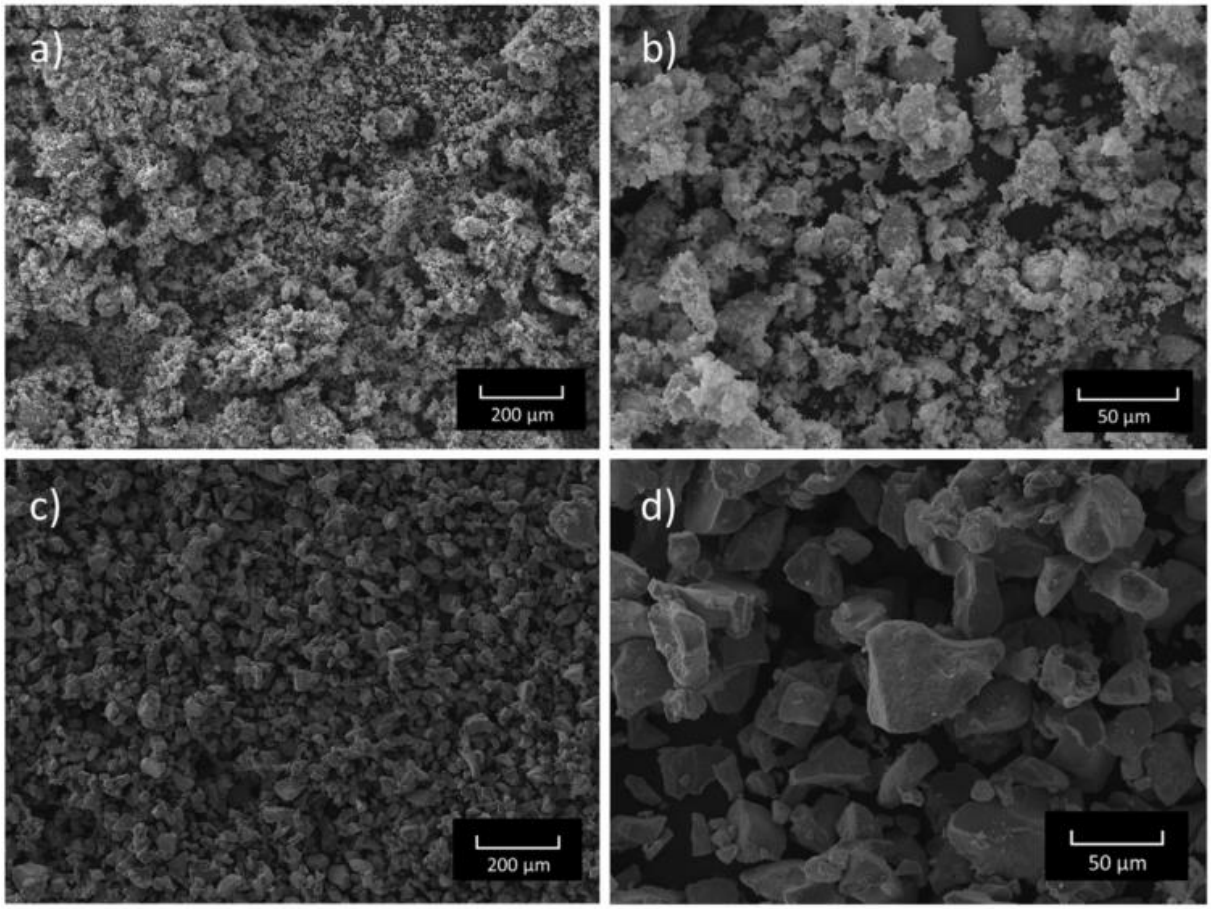

Fig. 41: SEM images of a, b) the LaSrMnO and c, d) the $La_{0.7}Sr_{0.3}(Fe_{0.2}Co_{0.8})O_3$ perovskite catalyst.

.

4.6.2 XRD

X-ray diffraction analysis was used for the verification of the phase purities of the prepared perovskite catalysts. The results are published by Grimmer et al. [61]. The XRD patterns confirm the existence of pure phase and the successful preparation of both catalysts with negligible impurities. The result is comparable to literature publications [63,64].

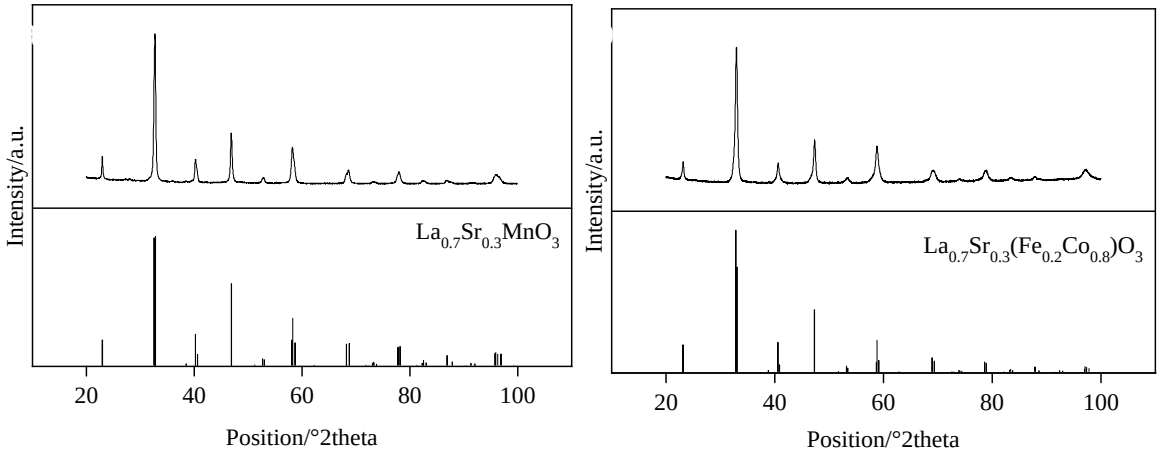

Fig. 42: Resulting patterns of the XRD analysis [61].

5 Conclusion

The aim of this work was to study two perovskite and one $AgMn_xO_y/C$ catalyst regarding their ability to catalyze the ORR for an alkaline DEFC. The high performance of all three catalysts in alkaline media was confirmed by ex-situ (RDE) characterizations and in-situ by half-cell measurements. In 6 M KOH, the $La_{0.7}Sr_{0.3}MnO_3$ catalyzed cathode exhibited the highest performance, with a current density of up to 685 mA/cm² at a potential of 0.6 V vs. RHE (without internal resistance corrections). The $AgMn_xO_y/C$ catalyst outperformed the perovskite catalysts at ex-situ RDE measurements. During in-situ experiments with ethanol, however, the $AgMn_xO_y/C$ cathode suffered from high degradation. The perovskite catalysts on the other hand, showed remarkable long term durability in alkaline media and in the presence of low ethanol concentrations (1 M). The $La_{0.7}Sr_{0.3}(Fe_{0.2}Co_{0.8})O_3$ perovskite electrode was in operation for 1,269 hours and provided, at the end of the measurement (after 1,150 hours in 1 M EtOH), still a current density of 160 mA/cm² at a potential of 0.6 V vs. RHE with oxygen as feed gas. Long-term measurements of the $La_{0.7}Sr_{0.3}MnO_3$ indicated a similar durability. For stability reasons, a PTFE concentration between 15 and 20% proved to be beneficial for the perovskite catalysts. The PTFE amount plays a key role in the formation of the three phase boundaries, what makes it mainly responsible for the electrode stability and soaking behavior.

Additionally, influences of the gas flow rate, oxygen partial pressure, temperature and electrolyte concentration were investigated. Following conclusions were drawn in order to improve the cathode and thus the fuel cell performance.

- An increase of the flow rate can be used to overcome a possible GDL wetting and to improve mass transfer. But, as shown in the measurements, this has only a minor impact on the performance (about 7-15% performance increase by doubling the flow rate), as long as no diffusion limitations are occurring.

- Another way to improve the cell performance is the switchover to pure oxygen. This increases the oxygen partial pressure and reduces the competition in the three phase boundary caused by inert gases from ambient air. Switching from air to oxygen provided the highest performance improvement of 300-400%, but might also be inappropriate for practical applications.

- A temperature increase improves not only the conductivity of the electrolyte, it also enhances the reaction kinetics at both electrodes significantly. The measurements revealed improved performances of around 20-40% by a temperature increase from 25° C to 45° C.

- The electrolyte concentration plays an important role. For ORR half-cell measurements, it seem to be advisable to use higher KOH concentration (at room temperature around 6 M) to benefit from the increased mass transfer and low resistance. But in full cell applications, a dominance of hydroxide ions at active anode catalysts sides should be avoided.

- The electrolyte and ethanol concentration must be balanced due to the competitive occupation of active catalyst sides.

The fuel-cell measurements confirmed the suitability of the perovskite catalyst to operate under fuel-cell conditions. Initial peak power densities of 15-17 mW/cm² for operations at room temperature are good results comparable to literature [61,65].

The SEM investigations confirmed an increased crosslinking of the PTFE network after the sintering process. It could be shown, that the fuel cell operation, with a pumped electrolyte/fuel mixture, led to increased crack formation.

The XRD measurements approved the successful preparation of both perovskite catalysts in respect to the phase purity and impurities within a negligible range.

6 Appendix

6.1 Instruments

Battery Test System: by BaSyTec, type: CTS-Lab

Hydrogen Reference Electrode (RHE): by gaskatel, type: HydroFlex®

Muffle Furnace: by Elsklo, type: LNT15G; 1320 °C/5.5 kW

Ultrasonic Bath: by Bandelin Sonorex, type: RK 31; 0.2 A/230 V

Ultrasonic Finger: by hielscher, type: UP 400S; 4 A/200-240 V

Press: by Fontune; 20 t/300 °C

Potentiostat: by Gamry Instruments, type: Reference 600 (Software: Gamry In-struments Framework; version: 6.25)

Ring Disk Electrode Tip: by Pine Research Instrumentation, type: AFE5T050GC; glassy carbon area: 0.196 cm2, max. 3000 rpm

Rotator: by Gamry Instruments, type: RDE 710 Rotating Electrode

Platinized Titanium Rod: by Bank Elektronik Intelligent Controls

Scanning Electron Microscope: by Tescan, type: Vega3

Secondary Electron Detector: by Tescan, type: Low Vacuum Secondary Elec-tron Detector 500 PA; with N2 and vacuum up to 500 Pa (Software: VegaTC)

Energy Dispersive X-ray detector: by Oxford Instruments; type: INCA x-act (Software: Inca)

Sputter Coater (gold): by Cressington; type: 108 auto 4 Experimental 69

6.2 Materials and chemicals

Nitrogen: by Air Liquide; Alphagaz™ 1 N_2; ≥99.999%

Oxygen: by Air Liquide; Alphagaz™ 1 O_2; ≥99.995%

Synthetic Air: by Air Liquide; Alphagaz™ 1 Air; ≥99.999% (N_2 + O_2), O_2: 20 ± 1%

Alumina Suspension: by Buehler; MasterPrep® Alumina Polishing Suspension; 0.05 µm

Potassium hydroxide (for in-situ): by Sigma-Aldrich; pellets, ≥85%

Potassium hydroxide (for ex-situ): by Sigma-Aldrich; concentrate 1 mol, Fluka® Analytical for 1 L standard solution

Cobalt(II) nitrate hexahydrate: by Sigma-Aldrich; A.C.S. reagent, 98+%

Iron(III) nitrate nonahydrate: by Sigma-Aldrich; A.C.S. reagent, ≤ 99%

Lanthan (III) nitrate hexahydrate: by Sigma-Aldrich; A.C.S. reagent, ≤ 99%

Strontium(I) nitrate: by Sigma-Aldrich A.C.S. reagent, ≤ 99%

Manganese(II) nitrate tetrahydrate: by Sigma-Aldrich; A.C.S. reagent, 98+%

Silver(I) nitrate: by Sigma-Aldrich; 98+%

Citric acid: by Sigma-Aldrich; A.C.S. reagent ≤ 99.5%

Ethylene glycol: by Fluka Analytical, ≤ 99.5%

2-propanol: by Sigma-Aldrich, ≤ 99.8%

Nafion: by Quintech; Nafion solution 5 wt%, NS05

Acetylene black: by Alfa Aesar; Carbon Black, 99.9%+; 75 $m_2\ g^{-1}$

Nickel mesh: by BOPP; w=0.510 mm, d=0.150 mm, >99.7%

PTFE: 3M™Dyneon™PTFE by Dyneon

Vulcan carbon powder: VulcanXC72R by Cabot

Black Pearls carbon powder: Black Pearls 200 by Cabot

Ultrapure 18 MΩ H_2O

6.3 List of figures

6.4 List of tables

6.5 List of Abbreviations

AEM	Anion exchange membrane
AEMFC	Anion exchange membrane fuel cell
AFC	Alkaline fuel cell
Ag	Silver
AL	Active layer
Co	Cobalt
DEFC	Direct ethanol fuel cell
DLFC	Direct liquid fuel cell
DMFC	Direct methanol fuel cell
EIS	Electrochemical impedance spectroscopy
FC	Fuel cell
Fe	Iron
GDL	Gas diffusion layer
h	Hours
HHV	Higher heating value

HOR	Hydrogen oxidation reaction
HT-PEMFC	High temperature-polymer electrolyte membrane fuel cell
iR	Internal resistance
KOH	Potassium hydroxide
La	Lanthan
LHV	Lower heating value
MCFC	Molten carbonate fuel cell
N_2	Nitrogen
mp	Maximum power point
Mn	Manganese
ORR	Oxygen reduction reaction
PAFC	Phosphoric acid fuel cell
PEM	Polymer electrolyte membrane or proton exchange membrane
PEMFC	Polymer electrolyte membrane fuel cell
Pt	Platinum
PTFE	Polytetrafluorethylene
RE	Reference electrode
RDE	Rotating disk electrode
Rpm	Rotations per minute
Ru	Ruthenium
SEM	scanning electron microscopy
SOFC	Solid oxide fuel cell
Sr	Strontium
TEM	Transmission electron microscopy
UNFCCC	United Nations Framework Convention and Climate Change
WE	Working electrode
XRD	x-ray diffraction

7 Literature

[1] G.A. Schmidt, T.R. Karl, Annual Global Analysis for 2015 NASA 2015 Global Temperature, (2016).

[2] S. Arrhenius, in the Air upon the Temperature of the Ground, Philos. Mag. J. Sci. 41 (1896) 237–279.

[3] Properties - American Chemical Society, (n.d.). https://www.acs.org/content/acs/en/climatescience/greenhousegases/properties.html (accessed May 25, 2017).

[4] H. Rodhe, A Comparison of the Contribution of Various Gases to the Greenhouse Effect, Science (80-.). 248 (1990) 1217–1219. doi:10.1126/science.248.4960.1217.

[5] W. Cramer, A. Bondeau, S. Schaphoff, W. Lucht, B. Smith, S. Sitch, Tropical forests and the global carbon cycle: impacts of atmospheric carbon dioxide, climate change and rate of deforestation, Philos. Trans. R. Soc. B Biol. Sci. 359 (2004) 331–343. doi:10.1098/rstb.2003.1428.

[6] G. Koneswaran, D. Nierenberg, Global farm animal production and global warming: impacting and mitigating climate change., Environ. Health Perspect. 116 (2008) 578–82. doi:10.1289/ehp.11034.

[7] R. Heede, Tracing anthropogenic carbon dioxide and methane emissions to fossil fuel and cement producers, 1854–2010, (n.d.). https://link.springer.com/content/pdf/10.1007%2Fs10584-013-0986-y.pdf (accessed August 21, 2017).

[8] J. Cook, N. Oreskes, P.T. Doran, W.R.L. Anderegg, B. Verheggen, E.W. Maibach, J.S. Carlton, S. Lewandowsky, A.G. Skuce, S.A. Green, D. Nuccitelli, P. Jacobs, M. Richardson, B. Winkler, R. Painting, K. Rice, Consensus on consensus: a synthesis of consensus estimates on human-caused global warming, Environ. Res. Lett. 11 (2016) 48002. doi:10.1088/1748-9326/11/4/048002.

[9] G.S. Omenn, J. Holdren, D.E. Shaw, A. DE Treasurer Shaw, R.M. Bierbaum, J.E. Dowling, L. Enquist, S.S. Fitzpatrick James McDonnell Foundation Alice Gast, T.D. Pollard, P.R. Stang, K.D. Sullivan, AAAS Board Statement on Climate Change, (2006). https://www.aaas.org/sites/default/files/migrate/uploads/aaas_climate_statement.pdf (accessed May 26, 2017).

[10] R.B. Alley, T. Berntsen, N.L. Bindoff, Z. Chen, A. Chidthaisong, P. Friedlingstein, J.M. Gregory, G.C. Hegerl, M. Heimann, B. Hewitson, B.J. Hoskins, F. Joos, J. Jouzel, V. Kattsov, U. Lohmann, M. Manning, T. Matsuno, M. Molina, N. Nicholls, J. Overpeck, D. Qin, G. Raga, V. Ramaswamy, J. Ren, M. Rusticucci, S. Solomon, R. Somerville, T.F. Stocker, P.A. Stott, R.J. Stouffer, P. Whetton, R.A. Wood, D. Wratt, J. Arblaster, G. Brasseur, J.H. Christensen, K.L. Denman, D.W. Fahey, P. Forster, E. Jansen, P.D. Jones, R. Knutti, H. Le Treut, P. Lemke, G. Meehl, P. Mote, D.A. Randall, D.A. Stone, K.E. Trenberth, J. Willebrand, F. Zwiers, A report of Working Group I of the Intergovernmental Panel on Climate Change Summary for Policymakers Summary for Policymakers, IPCC Clim. Chang. (2007). http://www.ipcc.ch/pdf/assessment-report/ar4/wg1/ar4-wg1-spm.pdf (accessed May 25, 2017).

[11] T.E. Osterkamp, V.E. Romanovsky, Evidence for warming and thawing of discontinuous permafrost in Alaska, Permafr. Periglac. Process. 10 (1999) 17–37. doi:10.1002/(SICI)1099-1530(199901/03)10:1<17::AID-PPP303>3.0.CO;2-4.

[12] W. Haeberli, M. Beniston, Change Climate Permafrost and and in the Its Alps Impacts on Glaciers, Ambio. 27 (1998) 258–265. http://www.jstor.org/stable/4314732.

[13] J. Oerlemans, Extracting a Climate Signal from 169 Glacier Records, Science (80-.). 308 (2005) 675–677. doi:10.1126/science.1107046.

[14] G.-R. Walther, E. Post, P. Convey, A. Menzel, C. Parmesan, T.J.C. Beebee, J.-M. Fromentin, O. Hoegh-Guldberg, F. Bairlein, Ecological responses to recent climate change, Nature. 416 (2002) 389–395. doi:10.1038/416389a.

[15] IEA, World Energy Outlook 2016 Chapter 1, Iea. (2016) 28. https://www.eia.gov/forecasts/aeo/data/browser/#/?id=8-AEO2016&cases=ref2016~ref_no_cpp&sourcekey=0.

[16] UNFCCC. Conference of the Parties (COP), Adoption of the Paris Agreement. Proposal by the President., Paris Clim. Chang. Conf. - Novemb. 2015, COP 21. 21932 (2015) 32. doi:FCCC/CP/2015/L.9/Rev.1.

[17] A. Savaresi, The Paris Agreement: a new beginning?, J. Energy Nat. Resour. Law. 34 (2016) 16–26. doi:10.1080/02646811.2016.1133983.

[18] D. Bodansky, The Legal Character of the Paris Agreement, Rev. Eur. Comp. Int. Environ. Law. 25 (2016) 142–150. doi:10.1111/reel.12154.

[19] J. Larminie, A. Dicks, Fuel Cell Systems Explained, 2001. doi:10.1016/S0378-7753(00)00571-1.

[20] S.P.S. Badwal, S. Giddey, A. Kulkarni, J. Goel, S. Basu, Direct ethanol fuel cells for transport and stationary applications - A comprehensive review, Appl. Energy. 145 (2015) 80–103. doi:10.1016/j.apenergy.2015.02.002.

[21] FNR, Basisdaten Bioenergie Deutschland, Basisdaten Bioenergie Deutschl. 2014. (2014) 2–36.

[22] J.R. Varcoe, R.C.T. Slade, Prospects for Alkaline Anion-Exchange Membranes in Low Temperature Fuel Cells, Fuel Cells. 5 (2005) 187–200. doi:10.1002/fuce.200400045.

[23] Renewable Fuels Association » Industry Statistics, World Fuel Ethanol Production, (n.d.). http://www.ethanolrfa.org/resources/industry/statistics/#1454099103927-61e598f7-7643 (accessed June 21, 2017).

[24] THE EUROPEAN PARLIAMENT AND THE COUNCIL OF THE EUROPEAN, UNION, DIRECTIVE 2009/28/EC OF THE EUROPEAN PARLIAMENT AND OF THE COUNCIL, Off. J. Eur. Union. L 140/16 (2009). http://eur-lex.europa.eu/legal-content/EN/TXT/PDF/?uri=CELEX:32009L0028&from=EN (accessed June 21, 2017).

[25] G.A. Reinhardt, E. von Falkenstein, Environmental assessment of biofuels for transport and the aspects of land use Competition, Biomass and Bioenergy. 35 (2011) 2315–2322. doi:10.1016/j.biombioe.2010.10.036.

[26] L. Reijnders, M.A.J. Huijbregts, Biogenic greenhouse gas emissions linked to the life cycles of biodiesel derived from European rapeseed and Brazilian soybeans, J. Clean. Prod. 16 (2008) 1943–1948. doi:10.1016/j.jclepro.2008.01.012.

[27] Z. Zhang, L. Lohr, C. Escalante, M. Wetzstein, Food versus fuel: What do prices tell us?, Energy Policy. 38 (2010) 445–451. doi:10.1016/j.enpol.2009.09.034.

[28] M.D. Edgerton, Increasing Crop Productivity to Meet Global Needs for Feed, Food, and Fuel, Plant Physiol. 149 (2009). http://www.plantphysiol.org/content/149/1/7.short (accessed June 22, 2017).

[29] Communication from the Commission on the practical implementation of the EU biofuels and bioliquids sustainability scheme and on counting rules for biofuels, (2010). http://eur-lex.europa.eu/legal-content/EN/TXT/PDF/?uri=CELEX:52010XC0619(02)&from=EN (accessed June 22, 2017).

[30] L. An, T.S. Zhao, Y.S. Li, Carbon-neutral sustainable energy technology: Direct ethanol fuel cells, Renew. Sustain. Energy Rev. 50 (2015) 1462–1468. doi:10.1016/j.rser.2015.05.074.

[31] C. Lamy, E.M. Belgsir, J.-M. Le, Â. Ger, Electrocatalytic oxidation of aliphatic alcohols: Application to the direct alcohol fuel cell (DAFC), (n.d.). https://link.springer.com/content/pdf/10.1023%2FA%3A1017587310150.pdf (accessed July 24, 2017).

[32] N. Bizon, Improving the PEMFC energy efficiency by optimizing the fueling rates based on extremum seeking algorithm, Int. J. Hydrogen Energy. 39 (2014) 10641–10654. doi:10.1016/j.ijhydene.2014.04.194.

[33] R.P. O'Hayre, S.-W. Cha, W.G. Colella, F.B. Prinz, Fuel cell fundamentals, n.d. https://books.google.at/books?hl=de&lr=&id=O2JYCwAAQBAJ&oi=fnd&pg=PR11&dq=alkaline+fuel+cell+efficiency&ots=RQxNSUJZjk&sig=_7fm5p0WDDU5jVkbwgsFTTOHg_k#v=onepage&q=alkaline fuel cell efficiency&f=false (accessed August 22, 2017).

[34] S.P.S. Badwal, S.S. Giddey, C. Munnings, A.I. Bhatt, A.F. Hollenkamp, Emerging electrochemical energy conversion and storage technologies., Front. Chem. 2 (2014) 79. doi:10.3389/fchem.2014.00079.

[35] V. Bambagioni, C. Bianchini, Y. Chen, J. Filippi, P. Fornasiero, M. Innocenti, A. Lavacchi, A. Marchionni, W. Oberhauser, F. Vizza, Energy efficiency enhancement of ethanol electrooxidation on Pd-CeO 2/C in passive and active polymer electrolyte-membrane fuel cells, ChemSusChem. 5 (2012) 1266–1273. doi:10.1002/cssc.201100738.

[36] M.A.F. Akhairi, S.K. Kamarudin, Catalysts in direct ethanol fuel cell (DEFC): An overview, Int. J. Hydrogen Energy. 41 (2016) 4214–4228. doi:10.1016/j.ijhydene.2015.12.145.

[37] X. Ge, A. Sumboja, D. Wuu, T. An, B. Li, F.W.T. Goh, T.S.A. Hor, Y. Zong, Z. Liu, Oxygen Reduction in Alkaline Media: From Mechanisms to Recent Advances of Catalysts, (n.d.). doi:10.1021/acscatal.5b00524.

[38] W. Xia, A. Mahmood, Z. Liang, R. Zou, S. Guo, Earth-Abundant Nanomaterials for Oxygen Reduction, Angew. Chemie - Int. Ed. 55 (2016) 2650–2676. doi:10.1002/anie.201504830.

[39] S. Sui, X. Wang, X. Zhou, Y. Su, S. Riffat, C.-J. Liu, A comprehensive review of Pt electrocatalysts for the oxygen reduction reaction: Nanostructure, activity, mechanism and carbon support in PEM fuel cells, J. Mater. Chem. A. (2017) 1808–1825. doi:10.1039/c6ta08580f.

[40] F. Bidault, D.J.L. Brett, P.H. Middleton, N.P. Brandon, Review of gas diffusion cathodes for alkaline fuel cells, J. Power Sources. 187 (2009) 39–48. doi:10.1016/j.jpowsour.2008.10.106.

[41] J. Tulloch, S.W. Donne, Activity of perovskite La1-xSrxMnO3 catalysts towards oxygen reduction in alkaline electrolytes, J. Power Sources. 188 (2009) 359–366. doi:10.1016/j.jpowsour.2008.12.024.

[42] B. Wang, Recent development of non-platinum catalysts for oxygen reduction reaction, J. Power Sources. 152 (2005) 1–15. doi:10.1016/j.jpowsour.2005.05.098.

[43] C.Z. Guo, W.L. Liao, L.T. Sun, C.G. Chen, Synthesis of non-noble nitrogen-containing catalysts for cathodic oxygen reduction reaction: A critical review, Int. J. Electrochem. Sci. 10 (2015) 2467–2477.

[44] K. Elumeeva, J. Masa, J. Sierau, F. Tietz, M. Muhler, W. Schuhmann, Perovskite-based bifunctional electrocatalysts for oxygen evolution and oxygen reduction in alkaline electrolytes, Electrochim. Acta. 208 (2016) 25–32. doi:10.1016/j.electacta.2016.05.010.

[45] J. Suntivich, H. a Gasteiger, N. Yabuuchi, H. Nakanishi, J.B. Goodenough, Y. Shao-Horn, Design principles for oxygen-reduction activity on perovskite oxide catalysts for fuel cells and metal-air batteries., Nat. Chem. 3 (2011) 546–550. doi:10.1038/nchem.1069.

[46] T. Electrochemical, J. Suntivich, H.A. Gasteiger, N. Yabuuchi, Electrocatalytic Measurement Methodology of Oxide Catalysts Using a Thin-Film Rotating Disk Electrode The MIT Faculty has made this article openly available . Please share how this access benefits you . Your story matters . Citation Suntivich , Jin et al , (2015). doi:10.1149/1.3456630.

[47] K. Cammann, Instrumentelle analytische Chemie : Verfahren, Anwendungen und Qualitätssicherung, Spektrum, Akad. Verl, 2001. http://www.springer.com/de/book/9783827427397 (accessed December 19, 2017).

[48] J. Qiao, L. Xu, L. Ding, P. Shi, L. Zhang, R. Baker, J. Zhang, Effect of KOH Concentration on the Oxygen Reduction Kinetics Catalyzed by Heat-Treated Co-Pyridine / C Electrocatalysts, 8 (2013) 1189–1208.

[49] M. Cifrain, K. V. Kordesch, Advances, aging mechanism and lifetime in AFCs with circulating electrolytes, J. Power Sources. 127 (2004) 234–242. doi:10.1016/j.jpowsour.2003.09.019.

[50] S. Kim, T.D. Myles, H.R. Kunz, D. Kwak, Y. Wang, R. Maric, The effect of binder content on the performance of a high temperature polymer electrolyte membrane fuel cell produced with reactive spray deposition technology, Electrochim. Acta. 177 (2015) 190–200. doi:10.1016/j.electacta.2015.02.025.

[51] R.J. Gilliam, J.W. Graydon, D.W. Kirk, S.J. Thorpe, A review of specific conductivities of potassium hydroxide solutions for various concentrations and temperatures, Int. J. Hydrogen Energy. 32 (2007) 359–364. doi:10.1016/j.ijhydene.2006.10.062.

[52] P. Hydroxide, Electrical Conductivity Measurements of Aqueous and Immobilized, (2011).

[53] Y.S. Li, T.S. Zhao, Z.X. Liang, Performance of alkaline electrolyte-membrane-based direct ethanol fuel cells, J. Power Sources. 187 (2009) 387–392. doi:10.1016/j.jpowsour.2008.10.132.

[54] L. Wang, A. Lavacchi, M. Bevilacqua, M. Bellini, P. Fornasiero, J. Filippi, M. Innocenti, A. Marchionni, H.A. Miller, F. Vizza, Energy Efficiency of Alkaline Direct Ethanol Fuel Cells Employing Nanostructured Palladium Electrocatalysts, (2015) 2214–2221. doi:10.1002/cctc.201500189.

[55] E. De Geeter, M. Mangan, S. Spaepen, W. Stinissen, G. Vennekens, Alkaline fuel cells for road traction, J. Power Sources. 80 (1999) 207–212. doi:10.1016/S0378-7753(99)00072-5.

[56] I. Staffell, A. Ingram, Life cycle assessment of an alkaline fuel cell CHP system, Int. J. Hydrogen Energy. 35 (2010) 2491–2505. doi:10.1016/j.ijhydene.2009.12.135.

[57] T. Poux, A. Bonnefont, G. Kéranguéven, G.A. Tsirlina, E.R. Savinova, Electrocatalytic oxygen reduction reaction on perovskite oxides: Series versus direct pathway, ChemPhysChem. 15 (2014) 2108–2120. doi:10.1002/cphc.201402022.

[58] Q. Tang, L. Jiang, J. Qi, Q. Jiang, S. Wang, G. Sun, One step synthesis of carbon-supported Ag/MnyOx composites for oxygen reduction reaction in alkaline media, Appl. Catal. B Environ. 104 (2011) 337–345. doi:10.1016/j.apcatb.2011.03.007.

[59] Q. Wu, L. Jiang, L. Qi, L. Yuan, E. Wang, G. Sun, Electrocatalytic activity and stability of Ag-MnOx/C composites toward oxygen reduction reaction in alkaline solution, Electrochim. Acta. 123 (2014) 167–175. doi:10.1016/j.electacta.2013.12.125.

[60] P. Lolk, M. Bjerg, F. Allebrod, P. Lolk Mollerup, C. Chatzichristodoulou, M. Mogensen, Electrical conductivity measurements of aqueous and immobilized potassium hydroxide, (2011). http://orbit.dtu.dk/files/6368532/Electrical conductivity measurements.pdf (accessed December 20, 2017).

[61] I. Grimmer, P. Zorn, S. Weinberger, C. Grimmer, B. Pichler, B. Cermenek, F. Gebetsroither, A. Schenk, F.-A. Mautner, B. Bitschnau, V. Hacker, Ethanol tolerant precious metal free cathode catalyst for alkaline direct ethanol fuel cells, Electrochim. Acta. 228 (2017) 325–331. doi:10.1016/j.electacta.2017.01.087.

[62] N.R. Elezovic, B.M. Babic, L.M. Vracar, N.V. Krstajic, Oxygen reduction at platinum nanoparticles supported on carbon cryogel in alkaline solution, J. Serbian Chem. Soc. 72 (2007) 699–708. doi:10.2298/JSC0707699E.

[63] A.N. Petrov, V.I. Voronin, T. Norby, P. Kofstad, Crystal Structure of the Mixed Oxides La0.7Sr0.3Co1−zMnzO3±y(0≤z≤1), J. Solid State Chem. 143 (1999) 52–57. doi:10.1006/jssc.1998.8073.

[64] V.G. Sathe, S.K. Paranjpe, V. Siruguri, A. V Pimpale, Novel magnetic phases in : a neutron diffraction study, J. Phys. Condens. Matter. 10 (1998) 4045–4055. doi:10.1088/0953-8984/10/18/014.

[65] M.Z.F. Kamarudin, S.K. Kamarudin, M.S. Masdar, W.R.W. Daud, Review: Direct ethanol fuel cells, Int. J. Hydrogen Energy. 38 (2013) 9438–9453. doi:10.1016/j.ijhydene.2012.07.059.

[66] J.A. Curry, J.L. Schramm, E.E. Ebert, Sea Ice-Albedo Climate Feedback Mechanism, J. Clim. 8 (1995) 240–247. doi:10.1175/1520-0442(1995)008<0240:SIACFM>2.0.CO;2.

[67] A. Raval, V. Ramanathan, Observational determination of the greenhouse effect, Nature. 342 (1989) 758–761. doi:10.1038/342758a0.

[68] D.S. Arndt, M.O. Baringer, M.R. Johnson, State of the Climate in 2009, Bull. Am. Meteorol. Soc. 91 (2010) s1–s222. doi:10.1175/BAMS-91-7-StateoftheClimate.

[69] M. Hagen, D. Hanselmann, K. Ahlbrecht, R. Maça, D. Gerber, J. Tübke, Lithium-Sulfur Cells: The Gap between the State-of-the-Art and the Requirements for High Energy Battery Cells, Adv. Energy Mater. 5 (2015). doi:10.1002/aenm.201401986.

[70] K. Mazloomi, C. Gomes, Hydrogen as an energy carrier : Prospects and challenges, Renew. Sustain. Energy Rev. 16 (2012) 3024–3033. doi:10.1016/j.rser.2012.02.028.

[71] S.K. Hoekman, A. Broch, C. Robbins, E. Ceniceros, M. Natarajan, Review of biodiesel composition, properties, and specifications, Renew. Sustain. Energy Rev. 16 (2012) 143–169. doi:10.1016/j.rser.2011.07.143.

[72] A. Averberg, K.R. Meyer, C.Q. Nguyen, A. Mertens, A survey of converter topologies for fuel cells in the kW range, 2008 IEEE Energy 2030 Conf. ENERGY 2008. (2008). doi:10.1109/ENERGY.2008.4781012.

[73] A.E. Lutz, R.S. Larson, J.O. Keller, Thermodynamic comparison of fuel cells to the Carnot cycle, Int. J. Hydrogen Energy. 27 (2002) 1103–1111. www.elsevier.com/locate/ijhydene (accessed July 24, 2017).

[74] B. Wang, Recent development of non-platinum catalysts for oxygen reduction reaction, J.

Power Sources. 152 (2005) 1–15. doi:10.1016/j.jpowsour.2005.05.098.

[75] temperature KOH.pdf, (n.d.).